CHALMERS
UNIVERSITY OF TECHNOLOGY

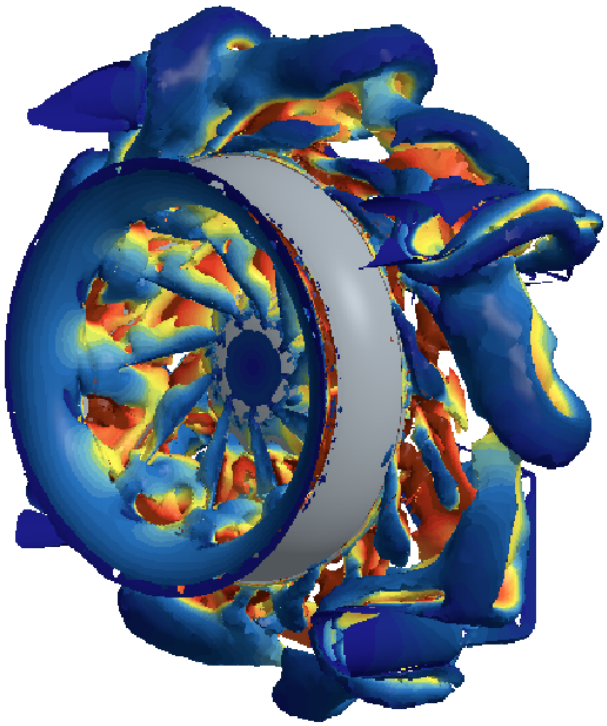

Numerical simulation of novel cooling fan concept for BEVs

Investigation of aerodynamic performance of novel cooling fan concept and comparison with conventional fan concept using Computational Fluid Dynamics

Master's thesis in Sustainable Energy Systems

LINUS FORSMAN
LUCAS HAMARD

Department of Mechanics and Maritime Sciences
CHALMERS UNIVERSITY OF TECHNOLOGY
Gothenburg, Sweden 2023
www.chalmers.se

Master's thesis 2023

Numerical simulation of novel cooling fan concept for BEVs

Investigation of aerodynamic performance of novel cooling fan concept and comparison with conventional fan concept using Computational Fluid Dynamics

LINUS FORSMAN

LUCAS HAMARD

CHALMERS
UNIVERSITY OF TECHNOLOGY

Department of Mechanics and Maritime Sciences
Division of Fluid Dynamics
Chalmers University of Technology
Gothenburg, Sweden 2023

Numerical simulation of novel cooling fan concept for BEVs
Investigation of aerodynamic performance of novel cooling fan concept and comparison with conventional fan concept using Computational Fluid Dynamics

LINUS FORSMAN
LUCAS HAMARD

Supervisor: Tobias Bergenblock, Volvo Car Corporation

Co-supervisor: Balachandra Tharanigere Raje Gowda, Volvo Car Corporation

Examiner: Lars Davidson, Department of Mechanics and Maritime Sciences

Master's Thesis 2023
Department of Mechanics and Maritime Sciences
Division of Fluid Dynamics
Chalmers University of Technology
SE-412 96 Gothenburg
Telephone +46 31 772 1000

Cover: Flow velocity profile visualization constructed in Simcenter STAR-CCM+ showing the outlet flow of a novel cooling fan concept.

Typeset in LaTeX
Printed by Chalmers Reproservice
Gothenburg, Sweden 2023

Numerical Simulation of novel cooling fan concept for BEVs
Investigation of aerodynamic performance of novel cooling fan concept and comparison with conventional fan concept using Computational Fluid Dynamics

LINUS FORSMAN
LUCAS HAMARD
Department of Mechanics and Maritime Sciences
Chalmers University of Technology

Abstract

The automotive industry is heading towards fully electric vehicles, Volvo Cars, itself, is aiming at becoming a fully electric car maker by 2030. With this change comes new challenges, and one of them is the development of the cooling fan. With battery electric vehicles, focus is put on efficiency, lower noise levels and fitting the operating range of the cooling fan to meet the cooling demand of battery packs. To meet these new requirements, a new cooling fan concept never used in passenger cars before is being investigated in order to replace the conventional axial fans still employed in the automotive industry nowadays.
In this thesis work, the purpose is to develop a CFD model of this novel fan concept in order to test the aerodynamic performance of the fan. The CFD simulations are performed in two different testing configurations, and the results obtained are then validated by comparing with data from testing conducted at Volvo and by the fan supplier. The same configurations are then simulated for the conventional axial fan in order to compare the performance of the two fan concepts. Finally, ram air simulations are done in order to understand the performance of the fan at different vehicle speeds.
The simulations are performed using a steady state solver together with the realizable k-ε turbulence model, and the fan is modelled with the Moving Reference Frame approach. The impact of using unsteady solver with fan modelled by Rigid Body Motion as well as the impact of using SST k-ω turbulence model are also investigated.
The results show a maximum deviation of less than 13% from the test data from supplier, which indicates that the model performs well. Regarding the comparison with axial fan, the results in open configuration show globally better performance and efficiency for the axial fan. However, the ducted configuration shows globally similar performance but better performance for the mixed flow fan at the points where the two fans will operate given a system of two radiators.
The main conclusion from this work is that mixed flow fan does not show really better performance with a system composed of two radiators, yet the vehicle is composed of more components that create pressure resistance and, in that case, the mixed flow fan presents some advantages in comparison to axial fan.

Keywords: Computation Fluid dynamics (CFD), Reynold averaged Navier-stokes equations (RANS), Star-CCM+, cooling fan, fan curve, Battery electric Vehicles (BEVs), aerodynamic performance

Acknowledgements

This thesis work has been conducted within the Thermal System Development team at Volvo Cars. First of all, we would like to express our gratitude to our supervisor Tobias Bergenblock for giving us the opportunity to perform this work and for his support and guidance throughout the entire project. We would also like to thank our co-supervisor Balachandra Tharanigere Raje Gowda for his availability, his support and for teaching us the most useful knowledge about CFD methods in STAR-CCM+. We are also thankful to Randi Franzke for giving us valuable advice on fan modelling, to Thomas Halsius for the design work made on the novel fan, to Hans Olsen for the testing work and to Brian Fechner for purchasing the fan. Thanks also to our group manager Helena Martini for her assistance over these five months.
Moreover, we would like to thank our university examiner Professor Lars Davidson for his precious discussions and feedback.
Finally, we would like to express a special thanks to our families for their limitless support during these two years of studies.

Linus Forsman and Lucas Hamard, Gothenburg, June 2023

List of Acronyms

Below is the list of acronyms that have been used throughout this thesis listed in alphabetical order:

BEV	Battery Electric Vehicle
CAD	Computer Aided Design
CFD	Computational Fluid Dynamics
DNS	Direct Numerical Simulation
ISO	International Organization for Standardization
LES	Large-Eddy Simulation
MRF	Moving Reference Frame
NS	Navier Stokes
RANS	Reynolds Averaged Navier-Stokes
RBM	Rigid Body Motion
RPM	Revolutions Per Minute
SIMPLE	Semi-Implicit Method for Pressure-Linked Equations
SST	Shear Stress Transport
VCC	Volvo Cars Cooperation

Contents

List of Figures

List of Tables

1
Introduction

1.1 Background

The automotive industry is heading towards fully electric vehicles and with this change comes new challenges. One of them is the development of the cooling system and specifically the cooling fan. With previous use of internal combustion engines, the cooling fan purpose were different. High demand of volume airflow to cool the engine using air/coolant heat exchanger was in the center of focus. With battery electric vehicles (BEVs) the focus is rather put on efficiency, lower noise levels and fitting the operating range of the cooling fan to meet the cooling demand of battery packs. Novel concept of cooling fans is therefore in the upcoming to investigate to match the new demands. To reduce cost and time for development and testing for a novel concept of a cooling fan, a robust numerical tool for aerodynamic performance is beneficial.

Numerical approaches for aerodynamic performance for air handling units, namely fans, have been used in decades and are currently in an advancing development with better computational resources. Choosing a proper numerical approach depends on application, requirement of result accuracy, availability of software and computational resources, and time.

1.2 Problem statement

The purpose of this thesis is to numerically, with use of Computational Fluid Dynamics (CFD), solve the aerodynamic performance of a novel fan concept for the thermal management system used in BEVs. Simulations results are validated with use of experimental data points from a fan test rig and comparisons are made with the existing fan concept used today.

1.3 Limitations

This master thesis project is limited to 20 weeks for two MSc students. Resources, such as software programs, computational resources and support are provided by Volvo Cars Cooperation (VCC).

1.4 Literature Review

Fans in general contribute to a considerable amount of the overall power consumption and a general goal is to reduce the consumption by making fans more efficient. In order to improve the aerodynamics for a fan one needs to look at the losses and find the range of potential improvement. Gebert [1] has found, with use of CFD and a baseline test for a state-of-the-art axial fan used in a wide operating range, a mechanical loss analysis. For the baseline test Gebert [1] found that out of 100% input shaft power, 32% are outlet losses measured as dynamic pressure that is not recover as static pressure at the fan outlet. About 1/3 of the outlet losses is tangential losses and 2/3 are meridional losses. Gebert [1] claims that one obvious solution to increase aerodynamic efficiency is to look at the outlet losses, he further explains that the state-of-the-art solution is to add diffusors to the existing fan to reduce the losses due to meridional losses and add guide vanes to reduce the tangential losses.

Studies from Shimada *et al.* [2] explain how and why axial fans has been and is still the dominant fan concept used in the automotive industry for engine cooling. Shimada *et al.* [2] further claim that due to high resistance from both heat exchangers and front grill on the upstream side of the fan as well as engine and engine auxiliaries on the downstream side of the fan, the purpose of the axial fan with axial discharge direction is somewhat lost as the discharge becomes more of the diagonal type. Shimada *et al.* [2] continue to explain that the trend in the automotive industry is smaller engine space and higher engine output leading to a significant increase in resistance both upstream and downstream of the cooling fan. Such an increase is forcing the fan to operate at a high static pressure and low air-flow state. Shimida *et al.* [2] further explain that tests show that, low- to medium air-flow rates lead to reversed flow close to the root of the blade causing the discharge to be diagonal and stating that it is obvious that a design of diagonal discharge is beneficial for aerodynamically purpose.

Studies made by Kawano and Fuchiwaki [3] evaluate the aerodynamic performance and noise mitigation for an axial fan in a cooling system. Kawano and Fuchiwaki [3] claim that the aerodynamic efficiency is worsened when the entire cooling system is not considered, in other words when the cooling fan performance is evaluated by its own. Efficiency is claimed to be worsen by a significant amount as the fan deviates from the maximum efficiency point.

However, Zhou *et al.* [4] explain the benefits of diagonal fans and how they are energy efficient and have a low noise level and that the fan industry is demanding them. But the development methodology of diagonal fans does not meet that demand, diagonal fan designs are mostly based on empirical data as traditional designs often requires a significant large amount of computational resources and focus has mostly been put on the application in the field of aeroengines for compressors with high speeds and high-pressure ratios. Zhou *et al.* [4] have developed a design optimization model for a diagonal fan and has found that diagonal flow fan has stronger work performance, less energy losses and a large increase in efficiency after

the optimization.

A study made by Franzke *et al.* [5] has evaluated two of the most common methods within CFD to simulate the rotating part of the fan, the moving reference frame and the rigid body motion methods. Franzke *et al.* [5] explain how moving parts is a great challenge within CFD as it requires movement of the mesh and parts, and thus, leads to computationally expensive and time-consuming simulations. Franzke *et al.* [5] have explained possibilities and limitations of the moving reference frame method. Users that are solving for temperature are advised to be cautious as the moving reference frame has limitations on capturing the physical nature of temperature fields. Moreover, Franzke *et al.* [5] have found that, for conventional axial fans, physical objects downstream of the fan have shown to impact the flow field upstream of the fan significantly.

2
Theory

In this chapter, a description of the theory used during the work is presented. First the governing equations used for the numerical simulations is introduces, followed by that the algorithms to solve the governing equations are described. Furthermore, modelling of turbulence is described. Modelling techniques specific for rotating regions is also described followed by theory for fan performance in general.

2.1 Governing equations

Fluid flows are an engineering challenge to solve and one can interpreter fluid flows at different scales. At the smallest of scales, at microscopic level, the flow is described at molecular level where collision of molecules takes place. However, for engineering tasks, the macroscopic scale is often considered where groups of molecules with uniform physical properties are divided into different grid elements. The fluid flow can therefore be modeled but with the loss of information at the smaller scales, which turns out to be one of the most challenging tasks for CFD applications [6].

At the macroscopic scale the fluid flow can be modeled with use of the three equations for continuity, namely, conservation of mass, conservation of momentum and conservation of energy [6].

The conservation of mass related the mass transport for a fluid and is described in equation (2.1).

$$\frac{\partial \rho}{\partial t} + \frac{\partial \rho U_j}{\partial x_j} = 0 \tag{2.1}$$

A common assumption used for several tasks within CFD is incompressibility, that is that the fluids density, ρ, stays constant within the computational domain. This is most often valid for lower speed flows. For incompressible flow, equation (2.1) can be simplified to equation (2.2)

$$\frac{\partial U_i}{\partial x_i} = 0 \tag{2.2}$$

The conservation of momentum, comes from Newtons second law of motion and relates the sum of forces acting on a fluid to its rate of motion, staying in incompressible flow:

$$\frac{\partial U_i}{\partial t} + U_j \frac{\partial U_i}{\partial x_j} = -\frac{1}{\rho}\frac{\partial P}{\partial x_i} + \frac{1}{\rho}\frac{\partial \tau_{ji}}{\partial x_j} + g_i \tag{2.3}$$

Energy within in fluid comes in many forms, as kinetic, thermal, chemical and potential energy. Depending on application, one can solve the energy source of interested. Equation (2.4) is for the conservation of total energy, which is mostly used in simulations where the temperature field is at interest [6].

$$\frac{\partial e}{\partial t} + U_j \frac{\partial e}{\partial x_j} = -\frac{1}{\rho} U_i \frac{\partial P}{\partial x_i} + \frac{1}{\rho} U_i \frac{\partial \tau_{ij}}{\partial x_j} + U_i g_i \tag{2.4}$$

Where e is defined as $e_i + e_k$, with e_i the internal energy and $e_k = \frac{1}{2}(U_1^2 + U_2^2 + U_3^2)$ the kinetic energy.

2.2 Numerical methods

The three conservation equations are non-linear equations including both spatial and temporal derivatives, making them difficult to solve analytically. Numerical methods are introduced to mathematically solve the governing equations. Finite volume method is one of the most broadly used numerical method to solve the governing equations. The finite volume method requires the computational domain to be discretized into many smaller volumes, which are referred to as mesh cells, or simply cells. In each cell the partial differential equation that should be solved, i.e. the continuity equations, can be simplified to linear algebraic equations that can be solved numerically. However, the result of discretization of the domain is numerical errors. The numerical errors need to be minimized to ensure accurate results. Decreasing the volume size of each cell usually leads to less error but also comes with an increase in computational time. The most important part of numerically solve the governing equations with the finite volume method is to find an accurate enough solution without a too heavy computational effort [6].

Equations (2.1), (2.3) and (2.4) can all be written in a more general form with the variable ϕ used as an arbitrary variable describing any fluid flow property. Following equation is used for simplification as it has the form of any transport equation.

$$\rho\frac{\partial \phi}{\partial t} + \rho\frac{\partial (u_j \phi)}{\partial x_j} = \frac{\partial}{\partial x_j}\left(\Gamma \frac{\partial \phi}{\partial x_j}\right) + S_\phi \tag{2.5}$$

In equation (2.5) the first term describes the temporal rate of change of property ϕ, second term describes the convective motion of ϕ, third term describes the diffusion of ϕ and lastly the fourth term is a source term [6].

Integrating equation (2.5) over a control volume, c.v., gives the following equation.

$$\int_{c.v.} \rho\frac{\partial \phi}{\partial t} dV + \int_{c.v.} \rho\frac{\partial (U_j \phi)}{\partial x_j} dV = \int_{c.v.} \frac{\partial}{\partial x_j}\left(\Gamma \frac{\partial \phi}{\partial x_j}\right) dV + \int_{c.v.} S_\phi dV. \tag{2.6}$$

After integration of the general transport equation Gauss' Theorem is applied. Gauss' Theorem states that a surface integral of a vector field taken over a surface surrounding a region is equal to the volume integral of the divergence over that region. By use of Gauss' Theorem, the convective and diffusive terms in the general transport equation can be written as

$$\int_{c.s.} \rho u_j n_j \phi dA \tag{2.7}$$

$$\int_{c.s.} \Gamma \frac{\partial \phi}{\partial x_j} n_j dA \tag{2.8}$$

respectively. Here n denoted the normal vector outwards from the cell, dA is the area surrounding the volume and $c.s.$ is the control surface which is the same as the surface that surrounds the cell. With the rewritten way of the integral form for the convective and diffusive term it makes it possible to solve the transport equation, if the transient term is disregarded, as it is for steady-state flow [6].

With the finite volume method equation (2.5) is solved for each of the corresponding fluid properties of interest at each cell. Each solution is then stored in the center of the cell [6].

Figure 2.1 shows a 1D representation of how discretization of a computational domain can be described. The figure can be used to simply show how the solution of property ϕ for point P can be found by accounting for integration from the west face, denoted w, to the east face, denoted e.

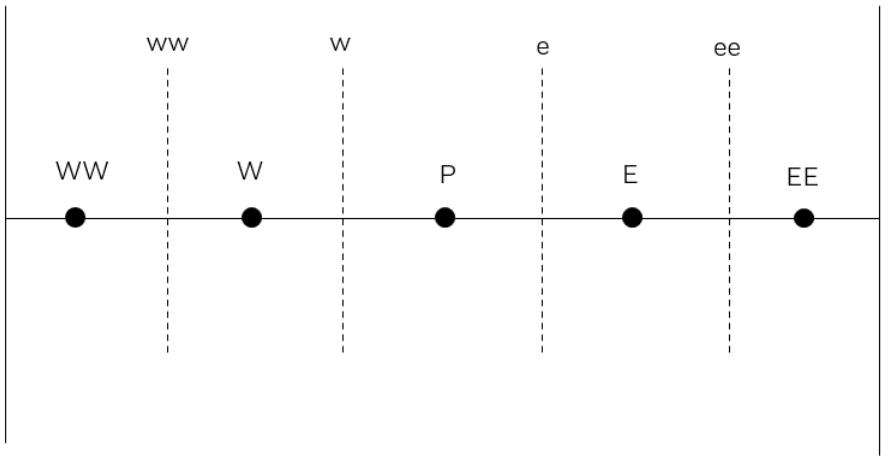

Figure 2.1: 1D representation of cells and cell faces

However, most often simulation requires more than one dimension and by defining a geometry by 3D mesh cells, one volumetric cell would have 6 faces. The 6 faces

can be denoted as w,e,s,n,t and b, corresponding to west, east, south, north, top and bottom. There is no real implementation of this notation but rather just used for simplification of the understanding of the numerical methods. In a structured grid, equation (2.7) and (2.8) can be evaluated to;

$$-\rho[(AU\phi)_w - (AU\phi)_e + (AV\phi)_s - (AV\phi)_n + (AW\phi)_t - (AW\phi)_b] \tag{2.9}$$

$$-\left[\left(A\Gamma\frac{\partial\phi}{\partial x}\right)_w - \left(A\Gamma\frac{\partial\phi}{\partial x}\right)_e + \left(A\Gamma\frac{\partial\phi}{\partial x}\right)_s - \left(A\Gamma\frac{\partial\phi}{\partial x}\right)_n + \left(A\Gamma\frac{\partial\phi}{\partial x}\right)_t - \left(A\Gamma\frac{\partial\phi}{\partial x}\right)_b\right] \tag{2.10}$$

respectively. The equations above are now solvable by simple algebraic methods. The values of ϕ, Γ and U_j as well as the gradient of ϕ is also needed at the faces. There are currently different ways of evaluating the central and face values, called schemes. The most obvious scheme is the centralized scheme which use linear interpolation of two adjacent cell values and assign it two a face. However, the influence of flow direction has been shown to have an impact of the numerical error and improved schemes has been generated to account for this [6].

2.2.1 First order upwind

By the impact of flow direction comes an important feature in numerical methods called transportiveness. Transportiveness is a desirable property in schemes and with the first order upwind schemes, flow properties are calculated using the same manners as previously described but the cell center values are projected to the downstream face, i.e. the cell center gets the value of the nearest upstream face [6].

$$\phi_w = \phi_W \tag{2.11}$$

$$\phi_e = \phi_P \tag{2.12}$$

2.2.2 Second order upwind

To increase accuracy even further from first order upwind scheme, the second order upwind scheme is used. Influence of two cells upstream is taken into account. This assumes that the gradient between present and eastern cell is equal to the gradient between western and present cell. This gives

$$\phi_e = 1.5\phi_P - 0.5\phi_w. \tag{2.13}$$

However, with better accuracy comes a drawback. The second order upwind scheme is unbounded. The value of a face does not necessarily lay in between the values of the cells used to estimate the face value. If the estimated face value lays outside the range of used cell values one can expect divergence and fast increase in numerical errors [6].

2.2.3 Temporal discretization schemes

Almost all flows are time dependent in reality but, for some engineering applications, they are disregarded for simplification or because only the non-time-dependent solution is of interest. For transient simulations, i.e., when the temporal derivative cannot be disregarded or when the transient nature of the flow is of interest, there should be a discretization of time. The whole transport equation for any flow property ϕ is integrated from the current time step t to $(t+\Delta t)$. To solve flow properties at the next time step there exists several schemes, two of them are the explicit discretization scheme and the fully implicit discretization scheme [6].

The explicit discretization scheme uses the solved fluid property at the previous time step to calculate the property at the current time step. This scheme requires a time step small enough to capture the change of properties within the fluid for each time step [6].

The fully implicit discretization scheme uses the flow property at a later time step. However, at later time step, the fluid property is not known, and thus inner sub-iterations is required for this scheme. For the fully implicit discretization scheme it is necessary to reach convergence by the inner sub-iteration for each time step [6].

2.2.4 Pressure-Velocity coupling

In previous sections it has been shown in a much simplified way that any arbitrary flow property can be solved using a number of different numerical schemes. The velocity is somewhat different. When the velocity field is unknown, which it is in almost all cases, a transport equation for momentum, i.e. the Navier-Stokes equations is needed. The Navier-Stokes equation has a source term including pressure gradient which makes it tricky to solve directly. Navier-Stokes equations and mass continuity equations, for incompressible flows, are expressed in equation (2.14) and (2.15) respectively.

$$\frac{\partial \rho U_i}{\partial t} + \frac{\partial \rho U_i U_j}{\partial x_j} = \frac{\partial}{\partial x_j}\left(\mu \frac{\partial U_i}{\partial x_j}\right) - \frac{\partial P}{\partial x_i}. \tag{2.14}$$

$$\frac{\partial \rho}{\partial t} + \frac{\partial \rho U_j}{\partial x_j} = 0. \tag{2.15}$$

For the case where velocity is unknown and should be solved, the sum of unknown variables in the continuity of mass and continuity of momentum are 4, namely 3 velocity components and pressure. Pressure cannot be solved with only usage of the equation for continuity of mass, meaning that the 3 equations for momentum cannot be used for solving the velocity component as it will leave pressure unknown [6].

Therefore, several iterative methods to solve pressure and velocity has been introduced. The most common is SIMPLE (Semi-Implicit Method for Pressure-Linked Equations). The SIMPLE algorithm uses starting guesses of velocity and pressure to solve for the velocities with use of the momentum equations. The starting guess for both velocity and pressure will not be correct and continuity is therefore not reached. A correction must be introduced. Transport equations for correction factors are introduced and solved for corrected velocity and pressure. The wanted properties are then solved again and convergence is measured to limit the numerical error. This iterative process continues until the user is satisfied with the numerical error [6].

2.3 Turbulence modelling

Turbulence is found all around the world for all kind of fluid flows, it is also very common in industrial applications and plays a significant role for mass and heat transfer. For aerodynamic flows, turbulence is often undesirable as it increases momentum transfer and greatly impacts skin friction which in turn increases drag. Turbulence is therefore of great interest to capture thoroughly. However, turbulence is very difficult to capture at a macroscopic scale and modeling of the phenomena is often required [6].

Flow consists of fluctuating velocities and other flow properties at all length and time scales. While Direct Numerical Simulation (DNS) captures all scales and Large-Eddy Simulation (LES) filters out the small scales, solvers based on Reynolds averaged Navier-Stokes equations (RANS-based solvers) filter out both small and intermediate-to-large time- and length scales. The widely used way of taking these scales into account is the Reynolds decomposition that decompose the instantaneous property into a mean and fluctuating part. The decomposition follows:

$$U_i = \langle U_i \rangle + u_i \tag{2.16}$$

$$P = \langle P \rangle + p \tag{2.17}$$

with,

$$\langle \phi \rangle = \frac{1}{\tau} \int_{t}^{t+\tau} \phi(x, \tilde{t}) d\tilde{t} \tag{2.18}$$

where τ is very large.

Substituting this decomposition into the governing equations gives:

$$\frac{\partial \langle U_i \rangle}{\partial x_i} = 0 \tag{2.19}$$

$$\frac{\partial \langle U_i \rangle}{\partial t} + \langle U_j \rangle \frac{\partial \langle U_i \rangle}{\partial x_j} = -\frac{1}{\rho}\frac{\partial \langle P \rangle}{\partial x_i} + \nu \frac{\partial^2 \langle U_i \rangle}{\partial x_j^2} - \frac{\partial \langle u_i u_j \rangle}{\partial x_j} \tag{2.20}$$

The right most term in equation (2.20) includes the average of nonlinear turbulent fluctuations, related to Reynolds stresses $-\rho\langle u_i u_j \rangle$, hence the equations are not closed and needs further modelling [6].

One way to close it is to use the Boussinesq approximation which states that "the transport of momentum by turbulence is a diffusive process and that the Reynolds stresses can be modelled using a turbulent viscosity, analogous to molecular viscosity. In contrast to the molecular viscosity, the turbulent viscosity is not a fluid property but depends strongly on the state of turbulence", which gives:

$$\frac{\tau_{ij}}{\rho} = -\langle u_i u_j \rangle = \nu_T \left(\frac{\partial \langle U_i \rangle}{\partial x_j} + \frac{\partial \langle U_j \rangle}{\partial x_i} \right) - \frac{2}{3} k \delta_{ij} \tag{2.21}$$

with k the turbulent kinetic energy defined as $k = \frac{1}{2}\langle u_i u_i \rangle$ and ν_t the turbulent viscosity that needs to be modeled [6].

This turbulent viscosity can be described as

$$\nu_T = C_\nu \frac{l^2}{t} = C_\nu u l \tag{2.22}$$

with u and l the velocity and length scales, and C_ν a constant.

To determine the turbulent viscosity, it is therefore needed to determine these two length scales. For that, it exists several ways which are characterized by the number of transport equations added to determine them [6].

In this thesis work, only two of the two-equations turbulence models are being used and will be presented in the following sections.

2.3.1 The realizable k-ε model

In this model, the turbulent kinetic energy k and the turbulent energy-dissipation rate ε are used to model the turbulent velocity and length scales. Solving the k equation enables to determine the velocity scale and solving the ε equation enables to determine the length scale. The relation between turbulent energy dissipation rate ε and turbulence length scale l being given by:

$$\varepsilon = \frac{k^{3/2}}{l} \tag{2.23}$$

The exact transport equation for the turbulent kinetic energy k is given by:

$$\frac{\partial k}{\partial t} + \langle U_j \rangle \frac{\partial k}{\partial x_j} = -\langle u_i u_j \rangle \frac{\partial \langle U_i \rangle}{\partial x_j} - \nu \left\langle \frac{\partial u_i}{\partial x_j} \frac{\partial u_i}{\partial x_j} \right\rangle + \frac{\partial}{\partial x_j} \left(\nu \frac{\partial k}{\partial x_j} - \frac{\langle u_i u_i u_j \rangle}{2} - \frac{\langle u_j p \rangle}{\rho} \right) \tag{2.24}$$

From this equation, several terms are unknown and, therefore, need closures in order to solve this equation [6]. These closures will not be detailed here, and the reader is referred to [6] for more information.
After substituting these closures, the modelled equation for k is given by:

$$\frac{\partial k}{\partial t} + \langle U_j \rangle \frac{\partial k}{\partial x_j} = \nu_T \left[\left(\frac{\partial \langle U_i \rangle}{\partial x_j} + \frac{\partial \langle U_j \rangle}{\partial x_i} \right) \frac{\partial \langle U_i \rangle}{\partial x_j} \right] - \varepsilon + \frac{\partial}{\partial x_j} \left[\left(\nu + \frac{\nu_T}{\sigma_k} \right) \frac{\partial k}{\partial x_j} \right] \tag{2.25}$$

In order to close the k equation, ε and the turbulent viscosity ν_T need to be calculated. As for the k equation, the ε equation contains unknown terms which need closures. Thus, after substitution of these closures, the modelled transport equation for the turbulent energy dissipation rate ε is given by:

$$\frac{\partial \varepsilon}{\partial t} + \langle U_j \rangle \frac{\partial \varepsilon}{\partial x_j} = C_{\varepsilon 1} \nu_T \frac{\varepsilon}{k} \left[\left(\frac{\partial \langle U_i \rangle}{\partial x_j} + \frac{\partial \langle U_j \rangle}{\partial x_i} \right) \frac{\partial \langle U_i \rangle}{\partial x_j} \right] - C_{\varepsilon 2} \frac{\varepsilon^2}{k} + \frac{\partial}{\partial x_j} \left[\left(\nu + \frac{\nu_T}{\sigma_\varepsilon} \right) \frac{\partial \varepsilon}{\partial x_j} \right] \tag{2.26}$$

The turbulent viscosity is, then, given by:

$$\nu_T = C_\mu \frac{k^2}{\varepsilon} \tag{2.27}$$

In these last two equations, C_μ, $C_{\varepsilon 1}$, $C_{\varepsilon 2}$, σ_k and σ_ε are closure coefficients that are assumed to be universal and constant (even if they can slightly vary between two different flows) [6].

Equations (2.25), (2.26) and (2.27) are the base equations for the standard k-ε model.

In the realizable k-ε model, a realizability constraint on the predicted stress tensor is featured to these equations. In the standard k-ε model, the normal stress can become negative.

Indeed, the normal stress tensor is equal to:

$$\langle u_i u_i \rangle = \sum_i \langle u_i^2 \rangle = \frac{2}{3} k - 2 \nu_T \frac{\partial \langle U_i \rangle}{\partial x_j} \tag{2.28}$$

So, it has to be larger than zero by definition. For that, the variable C_μ is no longer a constant (compared to the standard k-ε model but is a function of the local state of the flow to be sure to have a positive normal stress and, thus, ensure the realizability of the model [6].

The realizable k-ε model also adds a production term for turbulent energy dissipation which helps predicting the spreading rate for axisymmetric and planar jets. In general, this model is then better suited for flows with large strain rates [6].

The k-ε models, in general, are complete, give good results for many applications and are not so computationally expensive. The realizable k-ε model, in particular, gives improvement for simulations involving swirling flows and flow separation which are flows that can be found when simulating fans [6].

However, it is not as stable as the standard k-ε model, and the wall functions used in this model (see section 2.3.4) are not reliable for a lot of flows [6].

2.3.2 The SST k-ω model

In this turbulence model, the length scale is determined using the specific dissipation ω instead of ε with, by definition, $\omega \propto \varepsilon/k$.

The principal advantage of using the k-ω model is that, unlike the k-ε model, it does not need the empirical damping function in the viscous-sublayer. Thus, it gives better accuracy for flows with adverse pressure gradients and for separating flows [6].

The modelled transport equation for k remains unchanged compared to the realizable k-ε model except that ε is replaced by $\beta k\omega$, with β an empirical constant:

$$\frac{\partial k}{\partial t}+\langle U_j\rangle\frac{\partial k}{\partial x_j}=\nu_T\left[\left(\frac{\partial\langle U_i\rangle}{\partial x_j}+\frac{\partial\langle U_j\rangle}{\partial x_i}\right)\frac{\partial\langle U_i\rangle}{\partial x_j}\right]-\beta k\omega+\frac{\partial}{\partial x_j}\left[\left(\nu+\frac{\nu_T}{\sigma_k}\right)\frac{\partial k}{\partial x_j}\right] \quad (2.29)$$

The modelled transport equation for ω is, then, given by:

$$\frac{\partial\omega}{\partial t}+\langle U_j\rangle\frac{\partial\omega}{\partial x_j}=\alpha\frac{\omega}{k}\nu_T\left[\left(\frac{\partial\langle U_i\rangle}{\partial x_j}+\frac{\partial\langle U_j\rangle}{\partial x_i}\right)\frac{\partial\langle U_i\rangle}{\partial x_j}\right]-\beta^*\omega^2+\frac{\partial}{\partial x_j}\left[\left(\nu+\frac{\nu_T}{\sigma_\omega}\right)\frac{\partial\omega}{\partial x_j}\right] \quad (2.30)$$

And the turbulent viscosity is, then, given by:

$$\nu_T=\frac{k}{\omega} \quad (2.31)$$

In the same way as in the realizable k-ε model, β, α and β^* are constant closure coefficients [6].

Equations (2.29), (2.30) and (2.31) are the ones for the standard k-ω model. In the SST k-ω model, a blending function is used in order to apply the k-ε far from the wall in the free stream region and to apply the k-ω model near the walls [6].

If $\varepsilon = \beta k\omega$ is substituted in the energy dissipation equation of the k-ε model, then an equation for ω is obtained as:

$$\frac{\partial \omega}{\partial t} + \langle U_j \rangle \frac{\partial \omega}{\partial x_j} = \alpha \frac{\omega}{k} \nu_T \left[\left(\frac{\partial \langle U_i \rangle}{\partial x_j} + \frac{\partial \langle U_j \rangle}{\partial x_i} \right) \frac{\partial \langle U_i \rangle}{\partial x_j} \right] - \beta^* \omega^2 + \frac{\partial}{\partial x_j} \left[\left(\nu + \frac{\nu_T}{\sigma_\omega} \right) \frac{\partial \omega}{\partial x_j} \right] + 2 \frac{\rho \sigma_{\omega 2}}{\omega} \frac{\partial k}{\partial x_j} \frac{\partial \omega}{\partial x_j} \tag{2.32}$$

The last term is an additional term compared to the equation for ω in the k-ω model.

In the SST model, this last term in multiplied by (1-F_1) with F_1 a blending function that can take any value between 0 and 1.

F_1 is used so that near the wall $F_1 = 1$ (k-ω model used) and away from the wall $F_1 = 0$ (k-ε model used). In between, the blending function is creating a smooth transition between the two turbulence models [6].

It has also been noticed that for the k-ε and k-ω models, the wall shear stress is too high, and the flow does not separate from smooth surfaces. To solve that problem in the SST k-ω model, a viscosity limiter has been added. For that, another blending function F_2 is used.

Originally, $\mu_t = \frac{\rho k}{\omega}$ and in the SST model $\mu_t = \frac{a_1 \rho k}{max(a_1 \omega, S F_2)}$, with a_1 a closure coefficient, S the magnitude of the shear strain.

Similarly to F_1, F_2 is equal to 1 near the wall and equal to 0 away from the wall so that the turbulence viscosity is limited near the wall but stays the same away from it [6].

2.3.3 Turbulent boundary layers

A boundary layer is a region where the velocity increases rapidly from zero at the wall to the free-stream velocity. This is caused by the no-slip condition at the wall which implies that the relative velocity between the fluid and the wall is zero.
For turbulent flows, a corresponding turbulent boundary layer is obtained which can be divided into an outer region where the flow has a velocity almost equal to the free-stream velocity and an inner region where the velocity gradient is high [6].
This inner region is then divided into three sub-layers depending on the magnitude of both the viscous and turbulent parts of the total shear stress, τ_{xy},

$$\tau_{xy} = \rho \nu \frac{\partial \langle U_x \rangle}{\partial y} - \rho \langle u_x u_y \rangle \tag{2.33}$$

The no-slip condition implies that u_x, $u_y \to 0$ when y $\to 0$, so the turbulent shear stress is almost zero near the wall and then the total shear stress is only represented by the viscous shear stress, τ_w, at the wall,

$$\tau_w = \rho\nu \left.\frac{\partial\langle U_x\rangle}{\partial y}\right|_{y=0} \tag{2.34}$$

The physical variables at the wall can, thus, be defined using τ_w:

- The wall friction velocity:
$$u_* = \sqrt{\tau_w/\rho} \tag{2.35}$$
- The characteristic wall length scale:
$$l_* = \nu/u_* \tag{2.36}$$
- The non-dimensional wall distance:
$$y^+ = y/l_* = yu_*/\nu \tag{2.37}$$
With y the normal distance to the wall.

Then, from experiments, the inner region can be divided into:

- The viscous sub-layer for $0 < y^+ < 5$ (viscous stress dominant)
- The buffer sub-layer for $5 < y^+ < 30$ (viscous and turbulent stresses equally important)
- The fully turbulent sub-layer for $30 < y^+ < 400$ (turbulent stress dominant) [6]

2.3.4 Wall functions

One way of modelling the near-wall region is to use the wall-function approach. In this approach, the boundary conditions are applied away from the wall so that the turbulence model does not have to be solved close to the wall. In that way, it avoids using a dense mesh near the wall [6].
In the inner region, the mean velocity can then be defined as,

$$\langle U\rangle^+ = f(y^+) \tag{2.38}$$

In the viscous sub-layer, the turbulent stress being negligible, the following equation is obtained,

$$\frac{\tau_w}{\rho} = \nu\frac{\partial\langle U_x\rangle}{\partial y} \tag{2.39}$$

Knowing that the total shear stress is almost constant and equal to τ in the inner region, and applying the no-slip condition, it gives:

$$\langle U_x\rangle = \frac{\tau_w y}{\rho\nu} = \frac{u_*^2 y}{\nu} \tag{2.40}$$

which gives, in dimensionless form

$$\langle U_x \rangle^+ = y^+ \tag{2.41}$$

In the fully turbulent sub-layer, the viscous stress is negligible, and the characteristic length scale is proportional to the normal distance to the wall ($l = \kappa y$), the following equation is obtained,

$$\frac{\tau_w}{\rho} = -\langle u_x u_y \rangle = l^2 \left(\frac{\partial \langle U_x \rangle}{\partial y} \right)^2 = \kappa^2 y^2 \left(\frac{\partial \langle U_x \rangle}{\partial y} \right)^2 \tag{2.42}$$

which gives, in dimensionless form, after integration

$$\langle U_x \rangle^* = \frac{1}{\kappa} ln(y^+) + B \tag{2.43}$$

with κ and B two constants [6].

2.3.5 Two-layer wall treatment

Another way of modelling the near-wall region is to use the two-layer approach. In this approach, the wall-distance-based Reynolds number Re_y is taken into account,

$$Re_y = y \frac{\sqrt{k}}{\nu} \tag{2.44}$$

Then, the domain is divided into the fully turbulent region for $Re_y > 200$ and the viscosity affected region where $Re_y < 200$. In the fully turbulent region, the turbulence is solved by the same two-equation model that the one used in the outer zone. In the viscosity-affected region, a one-equation model is used to solve the turbulent kinetic energy and then the relation $\varepsilon = \frac{k^{3/2}}{l_\varepsilon}$ (with l_ε an appropriate length scale) is used to calculate the turbulent energy-dissipation rate [6].

A blending function can also be used to have a smooth transition between these two regions.

Unlike the wall function approach, the two-layer modelling enables to solve the governing equations in the near-wall region which improves the wall shear-stress calculation but it, thus, requires a very fine mesh in this near-wall region [6].

2.4 Fan Modelling

This section describes the different means to model the angular motion of the rotating part of the fan. There exist some fan models like the lumped fan model that is the only actual model out of the ones mentioned in this thesis. The lumped fan model uses interfaces at location of the fan blades instead of the physical blades. A fan curve obtained by experimental work is then applied at the interface to generate a corresponding mass flow. This is a straightforward approach that is relatively fast to get results from but can leave out important geometrical aspects, as for example the hub. The lumped fan model obviously requires a fan curve making it only fit for

simulations where one exists. For better accuracy and performing simulation where a fan curve is not present, other type of models are introduced [5].

2.4.1 Moving Reference Frame

Simulating a rotating domain comes with challenges, the moving reference frame, MRF, method originates from the idea that the mesh stays stationary, but the motion is defined to a reference frame. In the MRF, user-defined domains is set up to separate a stationary domain from a rotating domain where the information is transferred through interfaces between the domains. For steady-state simulations or in transient simulation that does not require time accurate result, the MRF suits well. The relative velocity, i.e., the velocity with respect to the moving reference frame, can be defined as:

$$v_r = v - v_{MRF,t} - \omega_{MRF} \times r_{P,MRF} \tag{2.45}$$

In equation (2.45), v is the absolute velocity i.e. the velocity relative to the laboratory frame, $v_{MRF,t}$ is the translation velocity of the moving reference frames origin (for rotating parts without any translation in x, y and z this term will be zero), ω_{MRF} is the angular velocity of the moving reference frame relative to the laboratory frame and $r_{P,MRF}$ is the position vector with respect to the moving reference frame [7].

Figure 2.2 shows the difference between the two reference frames. To the left the stationary reference frame is shown where the only rotating part is the fan which rotates with the rotational speed ω. To the right the moving reference frame is illustrated which shows that the frame of reference is rotating with the rotational speed ω.

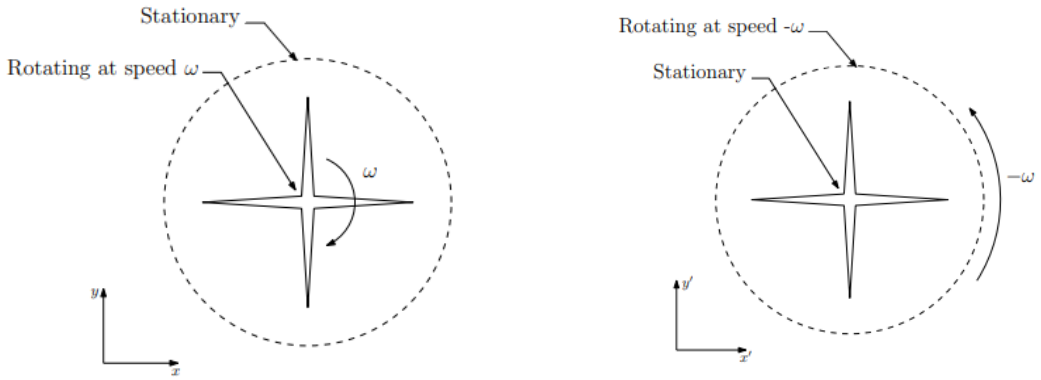

(a) Stationary

(b) Rotating

Figure 2.2: Comparison of MRF [8]

2.4.2 Rigid Body motion

Simulating a rotating domain and limit oneself to steady-state simulations can be insufficient. To better and more accurate capture transient phenomena the rigid body motion, RBM, is available in most CFD software. The RBM method keeps the mesh geometry at all times but allow the vertices to rotate and/or translate. Vertices in the rotating/translating domain will therefore move alongside the stationary domain resulting in a sliding motion against each other, that is why RBM is often referred to as "sliding mesh" approach [5][7].

The movement of vertices takes place at a certain user-defined time step, which should be limited to maximum on degree of rotation for each time step in order to ensure an accurate transfer of fluid properties across the interface that connect the two domains.

Computational wise, rigid body motion is heavier compared to moving reference frame as it requires time accurate solutions and hence requires solving the transient term in the governing equations [5].

2.5 Fan theory

This section covers the aspects of theory for fans in general, it covers the well-known fan curve, how the fan curve is interpreted and can be used for selection of fans. Fan efficiency is covered in this section as well.

2.5.1 Fan efficiency

To determine the efficiency of a fan the ratio between power to flow and the power input by the motor is commonly used. The power to flow is a measure of how much power is transferred to the airflow and is the product of the difference in static pressure between inlet and outlet of the fan and the volume flow rate at the inlet. The power input by motor is the product of moment and the rotational speed of the fan. This gives equation (2.46) that determines the efficiency of a fan [9].

$$\eta = \frac{\Delta p_s Q}{M\omega} \tag{2.46}$$

It should also be noted that efficiency can be calculated in several ways, fan impeller efficiency uses the mechanical power supplied to the impeller in the denominator, fan shaft efficiency uses the mechanical power supplied to the shaft, fan motor shaft efficiency uses the shaft output power from the motor, and overall fan efficiency without variable speed uses the electrical input power [9].

2.5.2 Fan performance curve

A widely used measurement of the performance of a fan is the fan performance curve, more commonly known as the fan curve. The fan curve tells the relationship

between pressure rise (can be both of the form of static pressure or total pressure, but most often the static pressure rise is used) and volumetric flow. The fan curve is generally obtained by a set of data points gathered from experimental test of the fan for a range of operation points from zero volumetric flow to where the pressure rise is negligible. The fan curve is gathered for a specified rotational speed, meaning that a single fan will have multiple fan curves for different rotational speed [10]. Figure 2.3 shows a plot of a fan curve

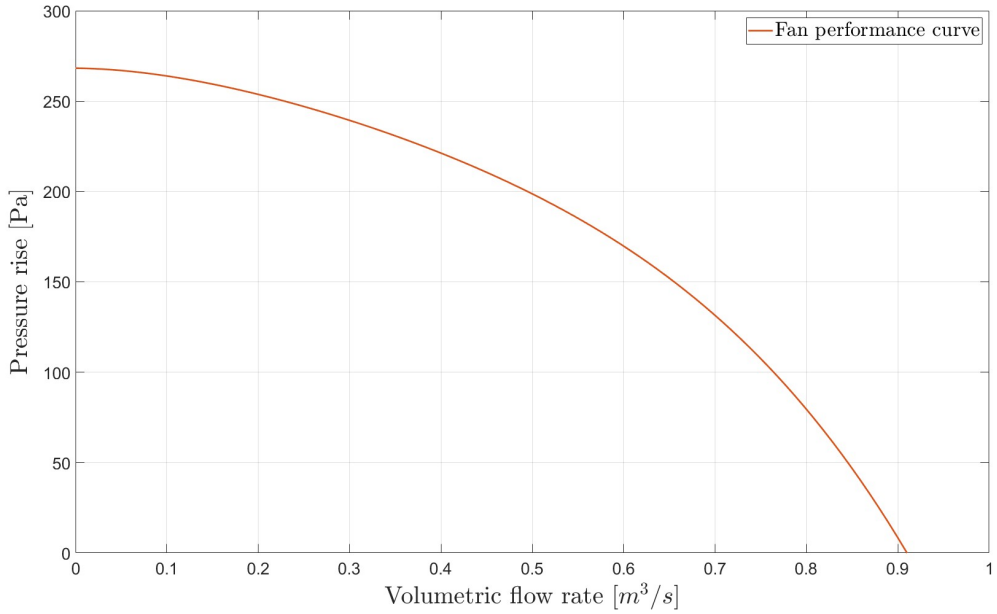

Figure 2.3: Example of a fan performance curve

The fan curve is often combined with the system curve. The system curve describes the resistance for a given system as the relation between static pressure and volume flow for that system. The relationship between pressure and volume flow for a system is a parabolic equation. Where the system curve and fan curve intersect is the region of interest. The intersection is the operating point. The operating point is the state of equilibrium between fan and system curve. The system curve, as with the fan curve, is most often obtained by experimental data obtained by test [10]. Figure 2.4 shows how system curve together with the fan curve is used to find the operating point.

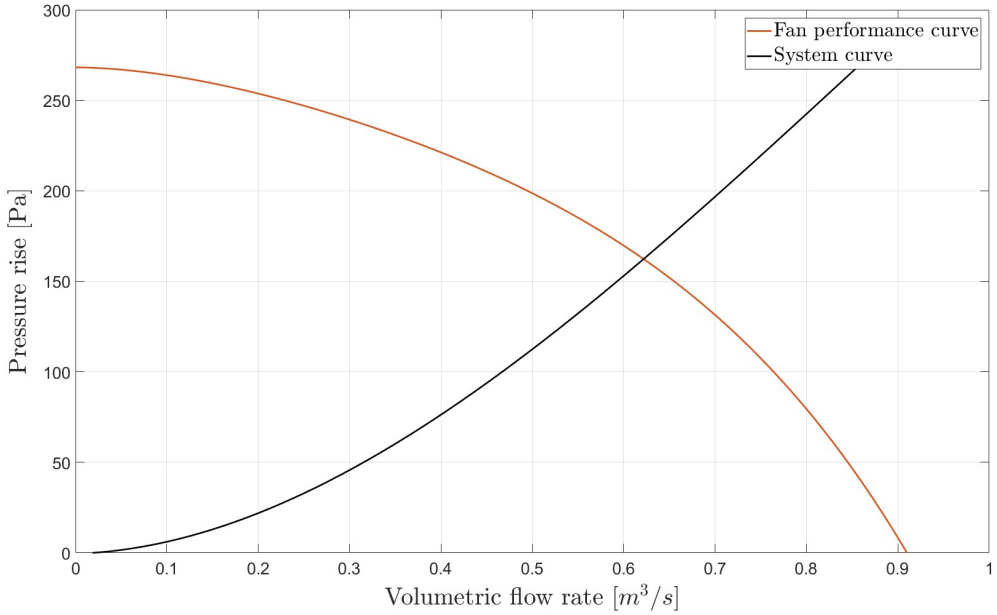

Figure 2.4: Example of a fan performance curve with intersecting system curve

It not always that the fan operates at the exact operating point but rather at conditions around it, this could be the cause of different volume flows acquired at a certain time. Changing rotational speed can adjust the operating point and thus give a range of operating conditions, thus an operating curve. Meeting the change in operating point can be made by alteration of the rotational speed for the fan as it will change the property of the fan curve [10].

As the operating region now can be distinguished by the system curve together with the fan curve, the efficiency for that operating region can also be gathered as a primary method of choosing a fan. The fan efficiency described in equation (2.46) is obtained as a function of volume flow and pressure rise for the fan. The efficiency curve can be plotted together with system- and fan curves. The intersecting point, i.e. the operating point/region should be aimed to have where the largest efficiency is obtained.

3
Methods

In this chapter the structure of the project is presented. The workflow is described in detail. The workflow consists of geometry preparation, process of settings up the computational domain, mesh independence study, CFD simulations as well as post-processing of results.

3.1 Project structure

The project structure consists of literature study, geometry preparation, mesh- and CFD study, simulations in CFD, validation of simulation results in comparison to experimental test results. and post-processing of simulation result.

Before the thesis started, a pre-thesis study has been conducted at Volvo in order to choose the right prototype for the mixed flow fan.

Then, at the beginning of this thesis, a literature study was conducted in order to find appropriate mesh settings, how to set up the computational domain using existing ISO-standards, challenges and/or benefits that can arise with the new concept of cooling fan and also boundary conditions of interest.

Moreover, a mesh independence study was conducted to make sure that the result from simulation was independent of the mesh density i.e., coarseness of the mesh cells.

When mesh independence is reached, simulations are done to generate the fan curves for both the existing fan and as well as the new concept.
Experimental test in a test rig is done simultaneously as simulations are done and finally validation of the simulation results is compared with the experimental results.

3.2 Pre-Thesis study

Before the thesis was started, a prototype for mixed flow fan has been purchased from a supplier. It has been chosen so that the pressure rises and flow rates it generates correspond to the usual pressure rises and flow rates generated by the conventional axial fan used in Volvo BEVs. The choice for this mixed flow fan concept was based on the benefits stated on Section 1.4, that is the increase in efficiency, but also and mainly the decrease in noise levels compared to axial fan.

The chosen prototype for the mixed flow fan can't be shown for confidentiality reasons, and the fan pictures in the rest of this report will be shown for the conventional axial fan only, as simulations have also been made for this axial fan in order to compare the performances of the two fan concepts.

3.3 Experimental setup

Experimental tests for the fan performance curve have been conducted by the supplier before purchasing the fan as well as by Volvo at the end of this thesis. The tests are done to have a second comparison between the two fan performance and are also used to confirm the results gathered from some of the simulations and is an important part of the work to be able to tell if the results are trustworthy or not. For the results from the CFD simulations and the results from the experimental tests to match it does require that the geometry and conditions such as boundary conditions, temperature, pressure and RPM are matching as close as possible.

Experimental tests are also used worldwide in order to be able to compare performance between different fans. As fans comes in large variations there should be uniform ways to measure their performance and thus a standard is required. The standard used for the experimental setup is "SS-EN ISO 5801:2017 (E)" [9]. The need for international Standard has been proven important and some of the features within a standard is,

- Installation Categories:

  Different fan categories exist and are separated by the connection. Connection to inlet/outlet duct affects fan performance and thus specification of category used are important. Categories are distinguished by the installation type, if they are ducted or not.

- Common Segments:

  Inlet- and outlet duct or chambers should have standardized dimensions for the airways to ensure consistency of test results.

- Test Results:

  Measurement and calculations should be consistent and specified. E.g. pressure should be measured a specified distance upstream of the fan etc.

3.3.1 Test configuration

Two different installation categories havr been used throughout the thesis work, category A and category D [9]. Category A is an open installation, i.e., it is not ducted but rather connected to open chambers. Category D is a ducted installation with both inlet- and outlet duct. The main idea behind use of the two different categories is that existing test data from the supplier for the novel fan concept is for the installation category D, and testing at Volvo is conducted in the installation category A. During testing in test rig the setup should match the ISO-standards and should also be used for creation of the computational domain in later step.

- Category A

  Installation category A is an open configuration i.e., it has both inlet- and outlet chambers. Following the standards with standardized inlet test chamber. The dimension used is shown in Figure 3.1

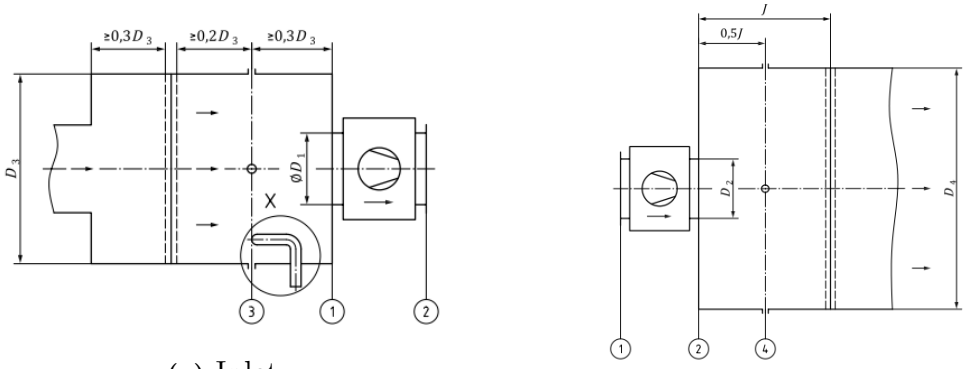

(a) Inlet

(b) Outlet

Figure 3.1: Category A [9]

  In the Figure, $D1$, is the hydraulic diameter of the fan at location 1. The standards states that the chamber cross-sectional area should be at least 5 times greater than the area of the fan inlet, i.e. $D3 > 5 * D1$. Pressure should be measured at the cross-section at location 3. The outlet fan diameter is located at location 2, the standard states that the outlet chamber cross-sectional area should be at least 9 times greater than the fan outlet area, i.e. $D4 > 9 * D2$. Pressure, if measured in the outlet chamber, should be measured the distance J away from the outlet of the fan. J is stated as $J > 2 * D2$ for discharge flow parallel to the axis of rotation.

- Category D

  Installation category D is a ducted configuration consisting of inlet- and outlet ducts. Figure 3.2 shows the inlet and outlet duct and the corresponding

dimensions.

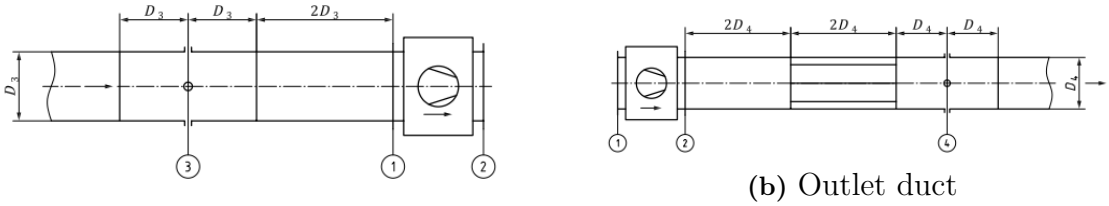

(a) Inlet duct

(b) Outlet duct

Figure 3.2: Category D [9]

The figure and standard states that the inlet- and outlet duct diameter should be the same as the corresponding inlet- and outlet fan diameter, $D3 = D1$ and $D4 = D2$. At the inlet side, pressure should be measured at location 3 in the figure, which corresponds to the distance $3 * D3$ away from the fan inlet, where the total distance of the duct is $4 * D3$. At the outlet side, pressure is measured at a distance $5 * D4$ away from the outlet of the fan, where the total distance of the duct is $6 * D4$. At a distance of $2 * D4$ a straightener can be used if needed.

However, to fulfill the ISO-standards. The outlet and inlet duct should also be connected to a inlet- and outlet common segment. The common segment used in this theses work is a "Long Duct". According to the standards a long duct should be at least $10 * D_{1,2}$. Figure 3.3 shows the dimensions of the used long ducts.

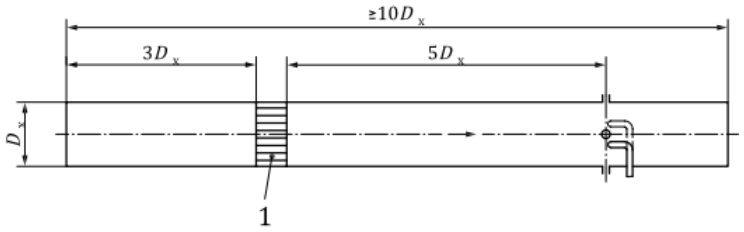

Figure 3.3: Dimensions for a long duct [9]

The tests are done for both existing fan used today and the mixed flow fan. Figure 3.4 shows the layout for the test rig. The pressure rise the fan generates are measured from the difference in pressure from the inlet pressure chamber, denoted 2, and outlet chamber, denoted 3 in Figure 3.4. Airflow is measured in the airflow measuring nozzles in the return circuit.

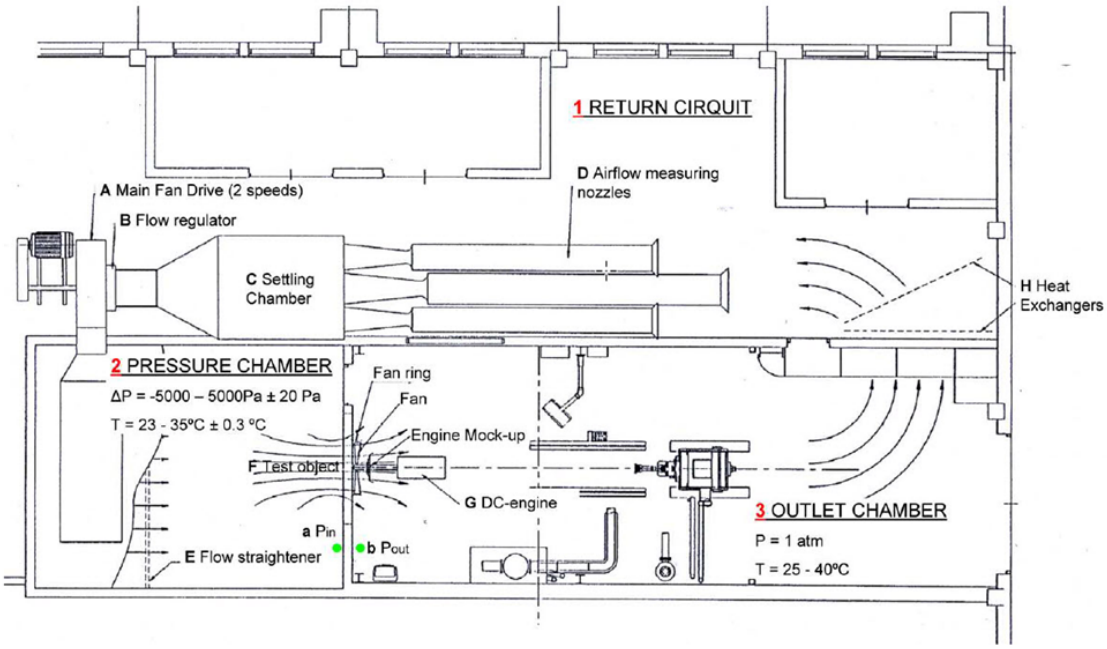

Figure 3.4: Sketch for test rig [11]

3.4 Geometry preparation

In order to get a computational domain and be able to execute aerodynamic simulations with CFD software's, there needs to be a representation of the geometry. The geometrical representation is made with help of computer-aided design, CAD. The CAD model has been provided at the beginning of the thesis. CAD files are generated in CATIA V5 and is used not only for aerodynamic simulations but also for other important steps in the concept phase such as assembly. As the many purposes with the CAD file, it needs to be matched and trimmed for the purpose of aerodynamic simulations and is therefore not yet ready to be imported to CFD programs but needs further pre-processing steps, consisting of geometry clean-up and geometry preparation. The CAD file is imported to the pre-processing program ANSA.

Geometry clean-up is made for simplification of the model, when the volume mesh is generated, small parts that does not impact the aerodynamic is unwanted. Example would be screws or details in the cooling pack that are so small that it would be difficult to capture the flow properties these details accurately and capturing the flow properties is not of interest at this region. Focus on removing unwanted part is therefore both of importance to mimic numerical errors at very fine geometrical spaces and to reduce the computational cost of generating surface- and volume mesh as well the computational cost of running the simulations.

Figure 3.5 shows an uncleaned geometry to the left and a cleaned geometry after pre-processing to the right. In the figure it can be seen that outside parts,

mainly used for assembling of cooling pack to the surrounding, which can be to parts within the car or to a test rig, has been removed. The purpose of this is both that these are completely unnecessary for the aerodynamics as almost all the airflow will pass through the fan and that the rest of the domain can easier be merged to the cooling pack when there is straight edges on the cooling pack. Furthermore, it is also important that all gaps on the cooling pack is fully covered, this is so that the airflow does not go through any holes with less resistance than the fan, example of this can be seen on the top right corner in yellow in Figure 3.5b where small holes are covered. In fan testing rigs these holes are taped for the same reason.

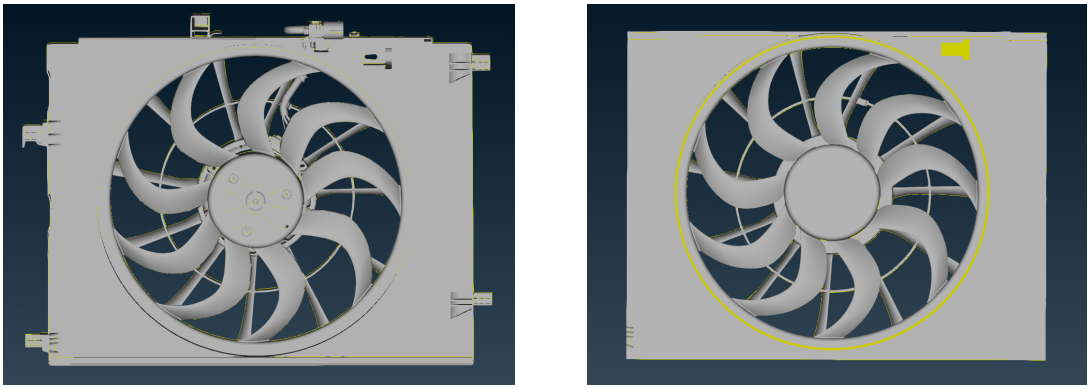

(a) uncleaned **(b)** cleaned

Figure 3.5: Geometry before and after cleaning

However, there is still regions within the main air-flow path that is needed to be removed as it will lead to unstable turbulent regions that are hard to capture with the numerical methods used. A zoomed in picture close to the fan hub is shown in Figure 3.6 shows clearly how smaller geometrical definitions are fully covered by more simple geometry representation. The airflow passes somewhat equal across the radii for most of fans meaning there will be somewhat of a large flow close to the hub that needs to be captured accurately to trust the results. Cleaning of geometry in region of interest and regions where the aerodynamic performance is impacted by the geometrical representation needs to be taken with caution. There will be a trade-off between accurately capturing the geometry and getting trustworthy results.

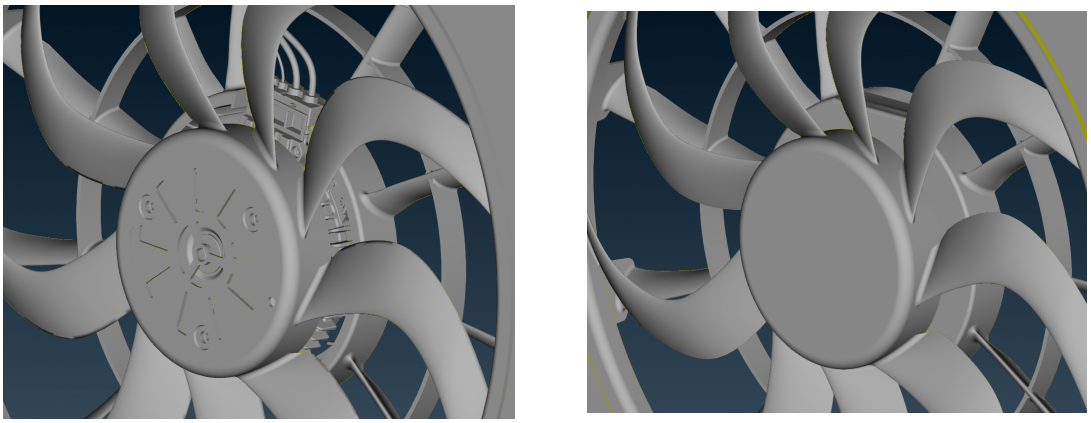

(a) uncleaned **(b)** cleaned

Figure 3.6: Geometry before and after cleaning

For most CFD simulations consisting of rotating parts the moving reference frame or rigid body motion is used. To do this the geometry needs to be divided into stationary- and rotating domains. This is also done in ANSA. Creating a rotating domain needs to be done so that it creates well defined interfaces between the domains. Furthermore, the interfaces should not intersect any stationary geometry parts as it will lead to unwanted rotation of the geometry. The rotating domain is made by creating an envelope surrounding the rotating fan plus the space close around the fan. The space available for creating such a domain is small. There are narrow distances between fan blades, shroud, cooling pack and motor that constraints the available space to create the domain. Furthermore, there should be available space for prism layers in addition to a few extra cells between any walls and a interface between the two domains. Figure showing the geometry of the rotating region is shown in section 3.5.

3.5 Computational domain

When the geometry is cleaned, i.e., when all holes are covered, all small geometry parts are approximated and when unnecessary parts are removed, the full domain needed for the CFD regions can be made. The complete domain consists of the cleaned fan model, inlet- and outlet air chambers or ducts (dependent on case), and inlet- and outlet boundaries.

Figures 3.7 and 3.8 show the computational domain for the two different configurations, open- and ducted configurations respectively, and that it can be divided into three main regions namely, inlet region, outlet region and rotating region.

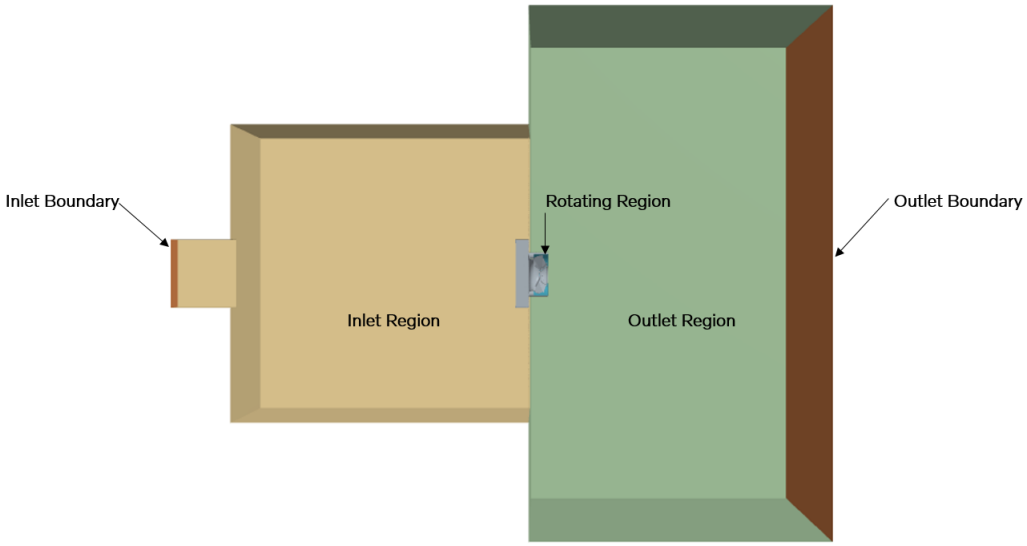

Figure 3.7: Computational domain for open configuration

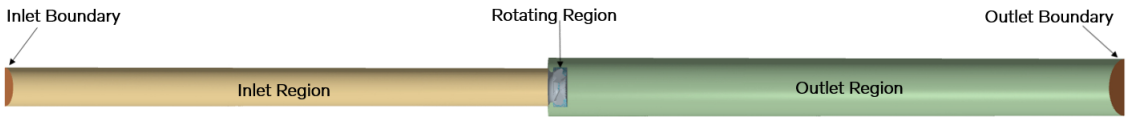

Figure 3.8: Computational Domain for ducted configuration

Furthermore, there is interfaces between the different regions to connect the regions to each other and distinguish them from walls. The regions were created in ANSA with respect to the dimensions described in section 3.4. Figure 3.9 shows a visualisation of the rotating region, in blue, that surrounds the fan.

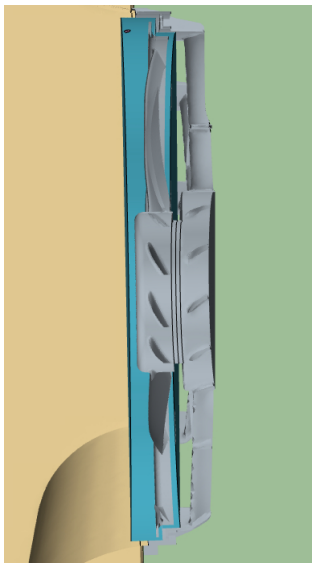

Figure 3.9: Rotating region surrounding the fan

When the geometry clean-up is done and the surface mesh is generated, the cleaned geometry is imported to the CFD analysis software used at Volvo Cars, Star-CCM+.

3.6 CFD settings

3.6.1 Physical models

In this section the physical models that have been chosen for all the simulations of this thesis work will be discussed.

Firstly, the fluid material has been chosen to be air with a constant density of 1.18415 kg/m^3 and constant dynamic viscosity of $1.85508 \times 10^{-5} Pa.s$. Indeed, an incompressible model can be chosen since, after calculation, the highest possible flow velocity obtained at the tip of the blade, considering all the cases, reaches a Mach number of 0.217 which is below the threshold for compressible flow.

Then, a three-dimensional segregated flow solver has been selected. Indeed, the segregated solver is using a pressure-velocity coupling algorithm in order to solve the governing equations as it is explained in the Section 2.2.4, and this pressure-velocity coupling is based on the assumption of incompressible flow which is assumed in this thesis work. Moreover, segregated solvers use less memory than coupled flow solvers, so for these two reasons, the segregated flow solver has been selected.

Regarding the turbulence model, the realizable k-ε model has been selected to start with, more especially the realizable k-ε model with a two-layer all y^+ wall treatment. This turbulence model selection is made from a previous thesis work made by Omar Fares [8] at Volvo Cars and for which it has been concluded that this turbulence model gives the closest results to test data for the axial fan.

Finally, a steady state solver has been chosen to begin with, and could, later, be changed to implicit unsteady (with use of sliding mesh modelling) if results are too far from test data or if the simulation does not converge with steady state solver.

Below is a summary of the models used in this thesis work:

Table 3.1: Physical models

Space	Three Dimensional
Material	Gas
Flow	Segregated Flow
Equation of State	Constant Density
Time	Steady
Viscous Regime	Turbulent (RANS)
Reynolds-Averaged Turbulence	Realizable K-Epsilon Two-Layer All y+ Wall Treatment

3.6.2 Surface Wrapping

A surface wrapper is a tool in STAR-CCM+ that is used to provide closed and non-intersecting surfaces when starting with a CAD file of poor quality.

Most of the time, the computational domain imported from ANSA still contains some geometrical issues such as intersecting faces, free edges or edges shared by more than two faces. The geometry can contain a large number of errors like that, it is therefore useful to use a surface wrapper so that it does not have to be fixed manually.

The stationary and rotating parts have to be wrapped independently as they are separated by an interface. Then, for each surface wrapper, several settings have to be chosen carefully so that the surface is captured accurately. The base size and surface curvature are two important settings in this thesis work in order to capture well the curvature of the blades.

An important focus has also to be put on the contact prevention so that two specific surfaces do not come into contact where they should not be in contact. This can happen for surfaces really close to each other.

3.6.3 Mesh generation

Once the surface wrapper is generated, the volume mesh can be generated. There are different meshers that can be selected in order to generate both the surface and the volume meshes. In this thesis work, three main meshers have been used:

- Surface remesher:

  The surface remesher is used to remesh the initial surface in order to improve its quality and optimize it for the volume mesh models that are going to be used.

- Core volume mesher:

  The polyhedral mesher is the one generating the core volume mesh, producing cells with polyhedral shape. Different core volume mesher exists such as tetrahedral or trimmed mesher.

- Prism layer mesher

  The prism layer mesher is used to generate orthogonal prismatic cells next to the surfaces in order to better capture the turbulent phenomena near the walls and, thus, have accurate results.

3.6.3.1 Core volume mesh

The polyhedral mesher has been used for all the simulations in this thesis work. The main advantage of using a polyhedral mesh is that it is requires around five times less cells for a given volume compared to tetrahedral mesh. Therefore, for a given number of cells, polyhedral mesh has a better accuracy than tetrahedral mesh. Compared to trimmer mesh, polyhedral mesh is better for handling multi-region domain for which conformal mesh is required at the interfaces. In a more general way, polyhedral mesh is more stable, less diffusive, and more accurate than tetrahedral mesh, and it is more suitable for complex geometries with turbulent and swirling internal flows. However, the generation of a polyhedral mesh is, thus, more computationally expensive compared to tetrahedral and trimmer meshes.

Two different meshes have been generated, one for the rotating domain and one for the stationary domain. In order to capture the most accurately possible the flow phenomena, a finer mesh has been generated where the flow properties are changing the most. Thus, the final mesh is finer in the rotating region as well as in the stationary region close to the fan. For that, a volumetric refinement has been created as shown in Figure 3.10. The rest of the stationary domain is coarser as the gradients of the different properties are much smaller in that region.

Moreover, some refinement has been made on the surface mesh at the interface between stationary and rotating regions in order to get a conformal mesh between the two regions, which means that the meshes have to be of the same size. The same refinement has been applied to the surfaces of the fan blades and hub, so that, by setting a volume growth rate of 1 inside the MRF region, the whole MRF domain is of the size of the surface and interface refinement. Thus, at the end, the mesh of

the MRF region has a base size of 3.5mm.

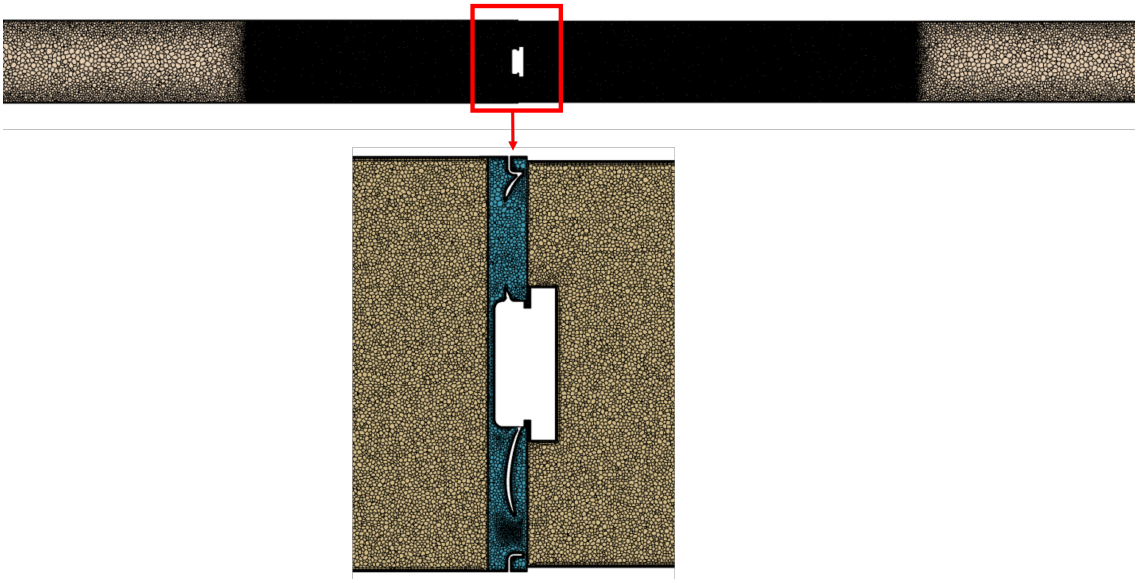

Figure 3.10: Mesh view with a closer look at the volumetric refinement

The mesh properties for the different cases studied in this thesis are presented in the following table:

Table 3.2: Mesh properties for the different study cases

Study case	Axial fan in open configuration	Axial fan in ducted configuration	Novel fan in open configuration	Novel fan in ducted configuration
Cell count	2.36 M	19.79 M	7.37 M	20.91 M
Number of faces	11.60 M	114.58 M	46.68 M	119.74 M

3.6.3.2 Prism layer

It has been proven that the realizable k-ε model, mainly used in this thesis work, requires $y^+ < 5$. It is also known that the k-ω model requires $y^+ \approx 1$. These two turbulence models being used in this thesis, the prism layer settings have been chosen so that y^+ respects this last condition.

In order to have $y^+ \approx 1$, the first prism layer thickness, also called "prism layer near wall thickness" in STAR-CCM+, has been set to 0.02mm.

Regarding the other prism layer settings, the last prism layer height has been aimed to be equal to the base size of the MRF domain (3.5mm) divided by the prism layer stretching factor in order to have a good transition between the prism layer and the core mesh. For that, 11 prism layers have been chosen with a total thickness of 5mm.

Regarding the prism layer on the interfaces, 1 prism layer with a total thickness of 1mm has been chosen in order to follow the standard settings for industrial models used at Volvo Cars.

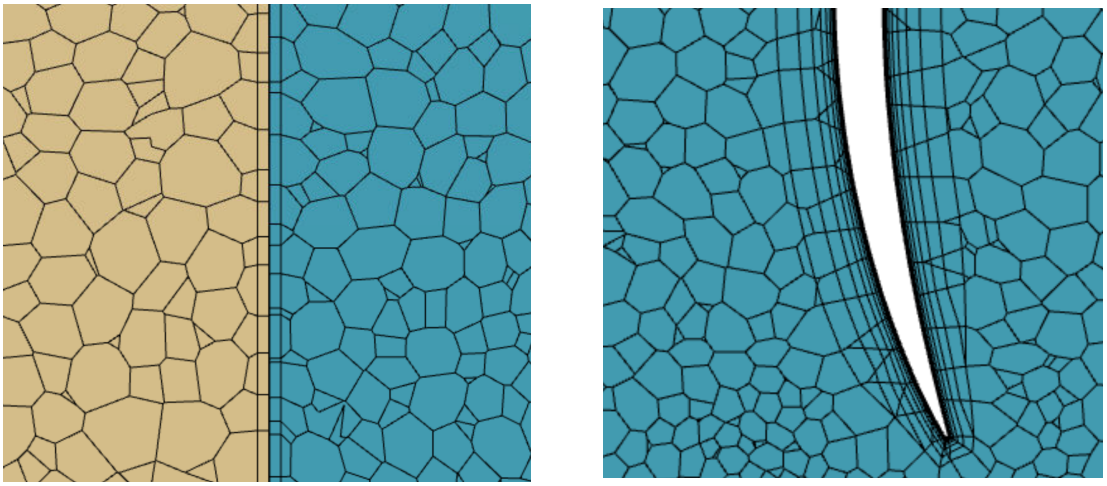

(a) At interfaces **(b)** At the walls

Figure 3.11: Prism layer at interfaces and walls

Figure 3.12 below shows the corresponding y^+ values at the fan blades for the generated prism layers. It can be seen that the average y^+ is around 1.

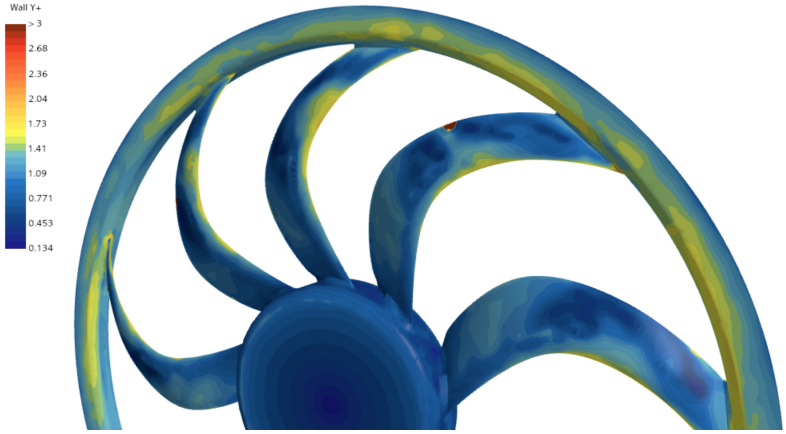

Figure 3.12: y^+ contour at the fan blades and hub

3.6.4 Boundary conditions

- Inlet boundary

Two different inlet boundary conditions have been used. Indeed, as it is discussed in Section 3.7, a mesh independence study has been conducted as a first step. For this, the mass flow has to be maintained constant for each iteration of the mesh study and a Mass Flow Inlet boundary has therefore been chosen.

As a second step, in order to generate the fan curve for each fan in the different configurations, a Pressure Inlet boundary (named Pressure Outlet in STAR-CCM+) has been chosen with pressure set to a value in the fan operating range in order to obtain the full curve.

- Outlet boundary

In all cases of this thesis work, a Pressure Outlet boundary has been chosen with the pressure set to 0 Pa (Gauge pressure) in order to respect the testing conditions for which the flow is released at atmospheric conditions at the outlet of the fan.

- Rotating region

As discussed earlier, Moving Reference Frame is first applied to the rotating region for steady state simulations, and then, if results are not accurate enough or not converged, a Rigid Body Motion (also called Sliding Mesh) is applied to the rotating region in order to run unsteady simulations and capture the transient phenomena.

The Moving Reference Frame is obtained by creating a rotating reference frame in STAR-CCM+ and setting the correct axis of rotation as well as the chosen rotational speed.

The Rigid Body Motion is obtained by creating a rotating motion in STAR-CCM+ and setting the correct axis of rotation as well as the rotational speed.

- Other faces

All the other faces of the computational domain are set to Wall with a no-slip condition. It concerns the faces of the stationary domain, but also the blades, hub, shroud, and rotor of the fan as well as the motor for cases where it is accounted for.

3.7 Validations of results

3.7.1 Fully ducted configuration

To ensure that the obtained results are reliable, a mesh independence study has first been carried out and a validation of the results has then been done by comparing them with the test data of the novel fan.

The original mesh was the coarsest one, it had a base size of 25mm for all the regions as well as a prism layer of 8mm total thickness composed of 11 layers with a stretching factor of 1.3.
Then, the mesh study has been conducted in several different steps:

- As a first step, a refinement has been made on the base size which has been

reduced to 20mm, then to 15mm and finally to 10mm (Iterations 1-4).

- As a next step, a volumetric refinement (see Figure 3.10) has been made as discussed in Section 3.6.3.1. This volumetric refinement has first been set to a size of 10mm and the volume growth rate on the MRF region is set to 1 so that every cells of these two regions have a size of 10mm (Iteration 5).

- Then, after some changes on the surface mesh and prism layer of the interfaces and of the walls inside the MRF region (see Section 3.6.3.1), the volumetric refinement has been decreased to a base size of 8mm, then to 6mm, 5mm and finally to 4mm (Iterations 6-9).

- As a last step, the base size of the MRF region has been set to 2.5mm (Iteration 10).

The parameter used to check the independence of the mesh is the static pressure at the inlet pressure plane (location 3 on Figures 3.1 and 3.2). The percentage of deviation between two refinement iterations is also checked, the goal being to have less than 1% deviation to consider the results independent of the mesh size.

The results can be seen in Figure 3.13 and Table 3.3 below:

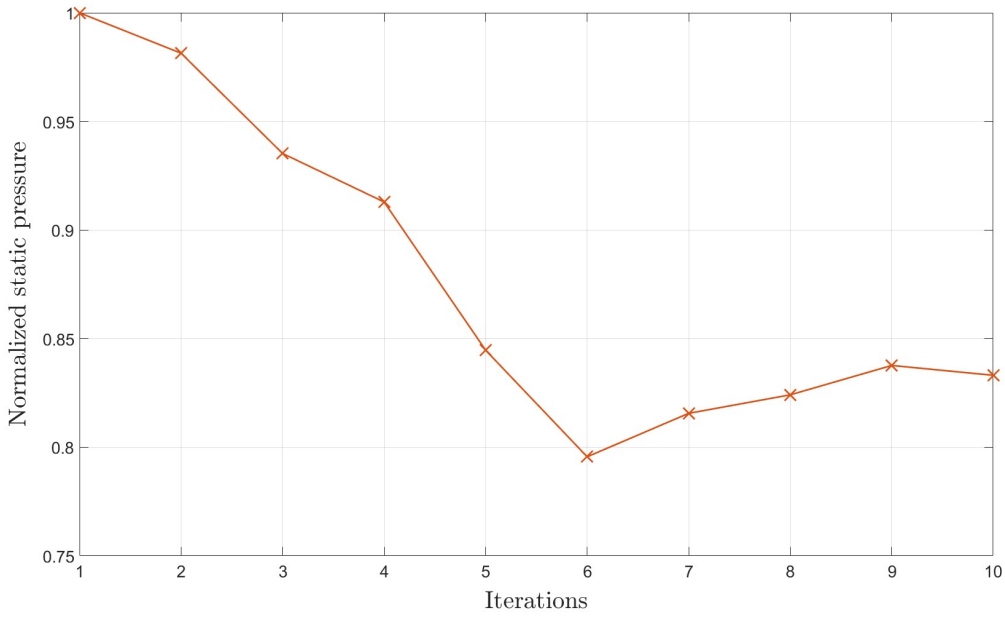

Figure 3.13: Normalized static pressure for the different iterations of the mesh study

Table 3.3: Normalized static pressure and deviation obtained for the different iterations

Iteration	Normalized static pressure	Deviation [%]
1	1	-
2	0.981	1.86
3	0.935	4.70
4	0.913	2.39
5	0.845	7.47
6	0.796	5.81
7	0.816	2.51
8	0.824	1.04
9	0.838	1.64
10	0.833	0.54

As it can be seen on the results, a deviation less than 1% is obtained between iterations 9 and 10. Thus, the mesh corresponding to iteration 9 has been chosen for the simulations made on this thesis work. More information about this mesh have been presented in Section 3.6.3.

The validation of the results has been carried out with the selected mesh for the whole fan operating range. The obtained results can be seen on Figure 3.14 and Table 3.4 below:

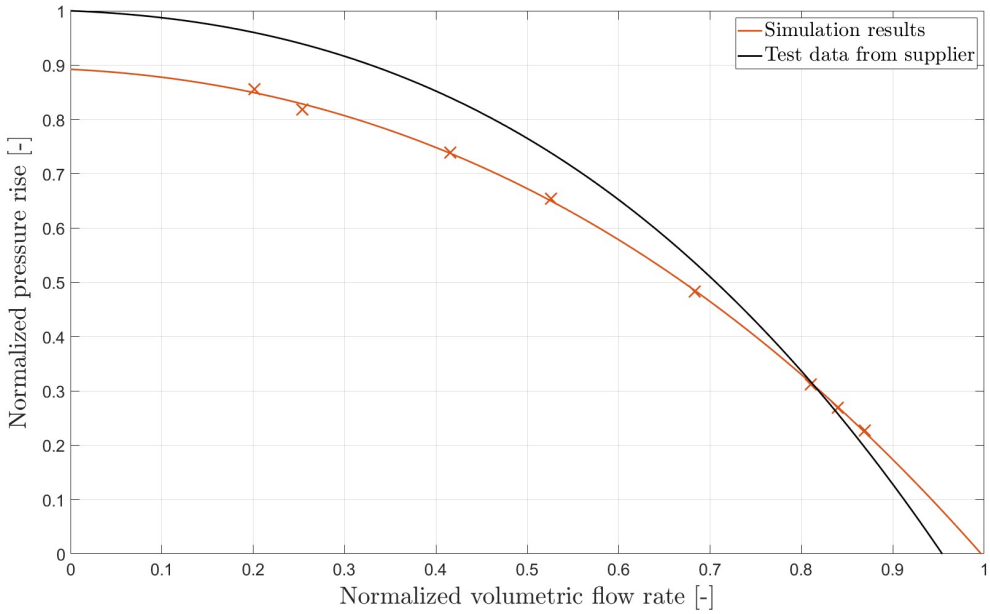

Figure 3.14: Normalized pressure rise from simulation and test data for different flow rates in ducted configuration

Table 3.4: Normalized pressure rise obtained from simulation and test data for different flow rates

Normalized flow rate	Normalized pressure rise from simulation	Normalized pressure rise from test data	Deviation [%]
0.20	0.893	1	10.67
0.25	0.854	0.981	12.93
0.42	0.772	0.882	12.53
0.53	0.683	0.766	10.86
0.68	0.504	0.553	8.92
0.81	0.325	0.342	4.89
0.84	0.281	0.274	2.46
0.87	0.237	0.193	22.81

As it can be seen on the results, the pressure rise obtained by the simulations is, in the majority of the cases, under a 13% deviation from the one obtained by the measurements. Only the case at 0.87 normalized flow rate has a higher deviation but this is not a problem since it is an extreme point, and those points are often extrapolated from actual measurements in the test data.

Therefore, since the simulation results are close enough to the test data, the rest of the simulations have been conducted with the same CFD settings as the one presented in this Section.

3.7.2 Fully open configuration

The same study has been conducted for the mixed flow fan in open configuration. The original mesh was generated with a base size of 20mm, a finer mesh of 10mm has been used for the stationary region around the fan and a mesh of 3.5mm has again been used for the MRF region.

From that mesh, a finer mesh has been created with all the cells 20% finer, that is 16mm base size and 8mm for the stationary region around the fan. Only the MRF region stayed to 3.5mm in order to respect the condition of 1 cell per degree of rotation.

A coarser mesh has also been created with cells 20% coarser, that is 24mm base size, 12mm for the stationary region around the fan and still 3.5mm in the MRF region.

The pressure at the inlet pressure plane is still the parameter used to check the mesh independence.

Simulations have been performed for these three meshes and the results can be seen in Table 3.5 below:

Table 3.5: Normalized static pressure and deviation obtained for the three meshes

Mesh	Normalized static pressure	Deviation [%]
Coarser	0.995	-
Intermediate	0.993	0.2
Finer	1	0.7

It can be seen that there is less than 1% deviation between the results of all the meshes which means that mesh independence is already achieved for the coarsest mesh. Therefore, this mesh has been chosen for the simulations made on this thesis work. More information about this mesh have been presented in Section 3.6.3.
The validation of the results has been carried out with the selected mesh for the whole fan operating range. The obtained results can be seen on Figure 3.15 below:

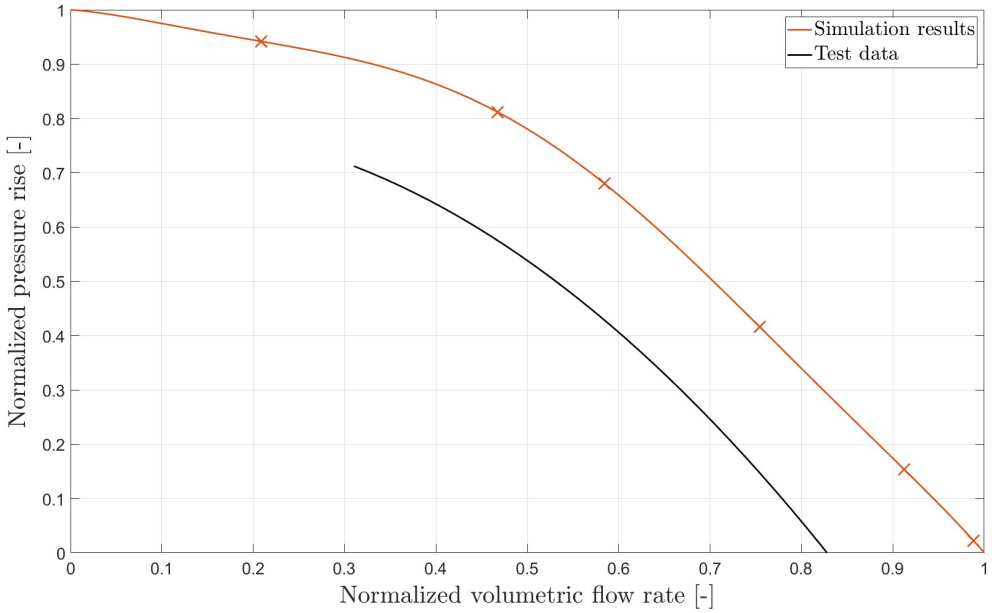

Figure 3.15: Normalized pressure rise from simulation and test data for different flow rates in open configuration

From this graph, it can clearly be seen that the deviation from simulation and test results is quite big and is not matching well. However, as the testing as been conducted during the last week of the thesis, this CFD model has been kept to run the simulations of the thesis. Moreover, the reasons for that deviation are still unknown and further investigations need to be made.

4
Results

In this chapter the results obtained from CFD simulations are presented. A first investigation on the impact of changing the turbulence model as well as the fan modelling approach is done. As a next step, the results for the two fan concepts are compared. And finally, ram air simulations are done in order to study the effect of vehicle speed on the mixed flow fan performance. The impact of downstream objects as well as sound measurements made during the fan testing have also been studied but won't be analyzed in this report for confidentiality reasons.

4.1 Impact of using the SST k-ω turbulence model

As specified in Section 2.3.2, the SST k-ω turbulence model is proven to be best suited for flows with adverse pressure gradients which is the case for flows through fans. Therefore, the impact of changing the turbulence model from Realizable k-ε to SST k-ω has been investigated.

For that, the boundary conditions have been set as usual, that is, a pressure inlet of a value in the operating range of the fan and pressure outlet of 0 Pa. For this simulation, the pressure inlet has been set to an intermediate pressure in order to get the fan running at a intermediate flow rate so that it avoids the extreme flow rates that would not be relevant for a comparison study.

The normalized pressure rise obtained together with the corresponding normalized pressure rise obtained with the k-ε model at the same flow rate can be seen on Table 4.1 below:

Table 4.1: Normalized pressure rise obtained for the different turbulence models

	Normalized pressure rise
Realizable k-ε	1
SST k-ω	0.998

From these results, it can be seen that only a 0.18% difference is obtained between realizable k-ε and SST k-ω models, that is almost no difference and that is the reason for which SST k-ω model has not been used more in this thesis work.

4.2 Impact of using the Rigid Body Motion approach

In this thesis work, the fans have only been modelled by using the Moving Reference Frame approach together with a steady state solver. However, most of the time, the Rigid Body Motion approach with unsteady solver turns out to be more accurate. This statement has, therefore, been investigated and the results are presented in this section.

The RBM simulation has also been conducted with the same boundary conditions used previously to generate the fan curves, that is, a pressure inlet of a value in the operating range of the fan, and a pressure outlet of 0 Pa. For this simulation, the pressure inlet has been set to an intermediate pressure for the same reason specified in the previous section.

The mixed flow fan is run at its maximum rotational speed, that is, 1750 rpm, and for the fan to turn one degree per time step, the time step has been set to $\Delta t = \frac{60}{360 \times 1750} = 9.52.10^{-5}\ s$.

The total simulation time is set to 0.17 s which corresponds to 5 fan revolutions, and the results are taken by averaging the variables over the last revolution. The normalized pressure rise obtained together with the corresponding normalized pressure rise obtained with the MRF approach at the same flow rate can be seen on Table 4.2 below:

Table 4.2: Normalized pressure rise obtained for the different approaches

	Normalized pressure rise
Moving Reference Frame	0.966
Rigid Body Motion	1

From these results, it can be seen that only a 4.4% difference is obtained between MRF and RBM approach, which can be considered as a too low difference to run simulations with RBM approach as it is a lot more computationally expensive. Indeed, one RBM simulation was approximately 3 times longer than a MRF simulation.

4.3 Comparison of axial and novel fan concept in open configuration

The next step is to investigate the mixed flow fan performance in comparison with the axial fan performance. To begin with, the two fans have been simulated in the open configuration and the fan performance curves have been obtained for both of them run at their maximum rotational speed, that is 2964 rpm for the axial fan and 1750 rpm for the mixed flow fan. This would correspond to a comparison between

the two fan concepts for similar motor power as the tests conducted by Volvo are done it that way. The generated fan curves can be seen on Figure 4.1 below:

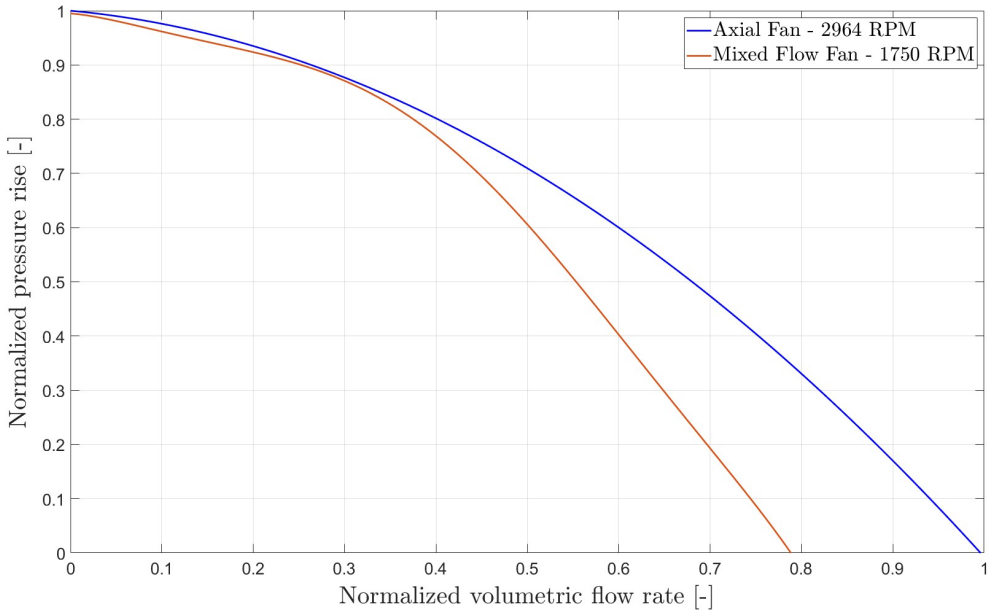

Figure 4.1: Normalized fan curves for axial- and mixed flow fan in open configuration

It can be clearly seen that, in this configuration, the axial fan can generate a higher pressure rise than the mixed flow fan for all the flow rate of the operating range. For low flow rate, the performance is quite similar for the two concepts, but the performance of the mixed flow fan starts decrease after that point. Moreover, the axial fan can operate for higher flow rates than the mixed flow fan.

The efficiency curve for both fans has also been generated as it can be seen in Figure 4.2 below:

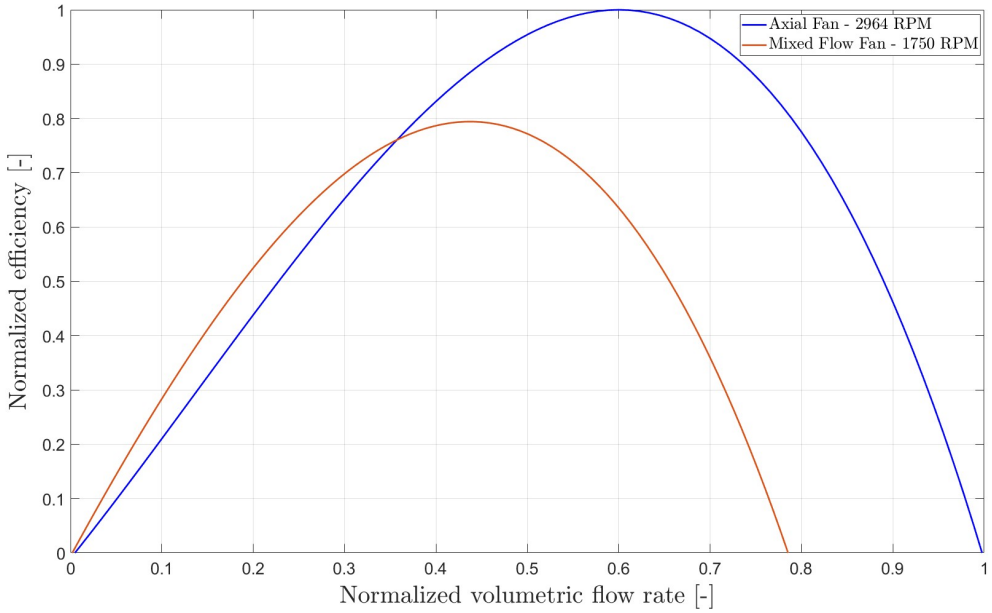

Figure 4.2: Normalized efficiency curves for axial- and mixed flow fan in open configuration

As it can be seen, in open configuration, the axial fan has a peak efficiency which is obtained at a normalized flow rate of 0.45 and which is around 20% higher than the peak efficiency of the mixed flow fan obtained at a normalized flow rate of 0.6.

Also, in the majority of the operating range, the axial fan has a higher efficiency than the mixed flow fan. However, it does not necessarily mean that the axial fan performs better than the mixed flow fan. To be able to tell that, the system curve has to be plotted together with the fan curves and the efficiency curves. Indeed, by doing that, the operating point can be found for both fan concept and the corresponding efficiency can be determined. All these curves can be seen in Figure 4.3 which shows the previously shown fan curves together with the efficiency curve for the fans. The pressure rise is read on the primary y-axis on the left-hand side while the efficiency is read on the secondary y-axis on the right-hand side.

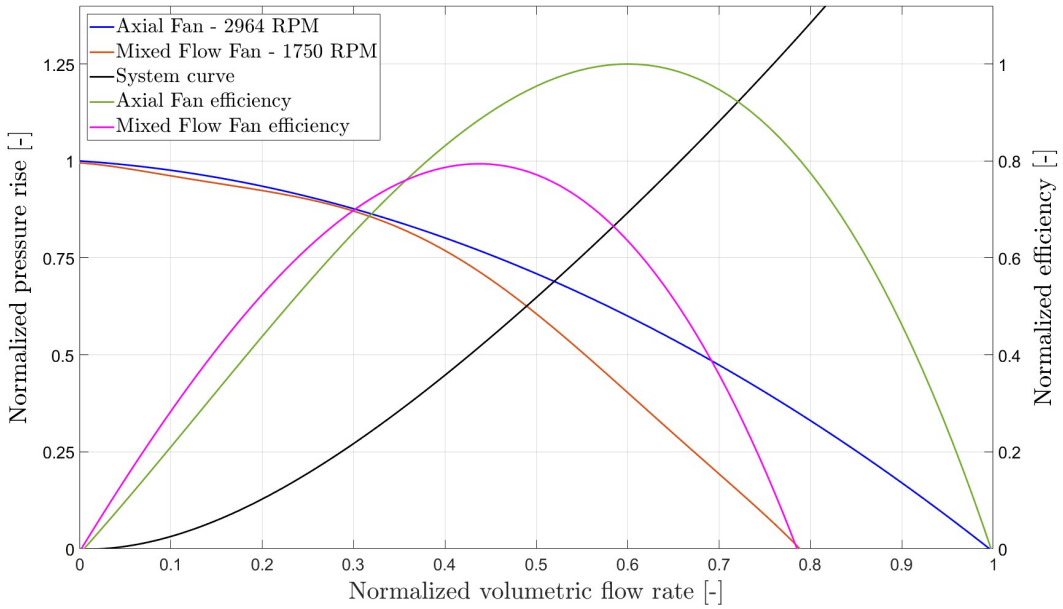

Figure 4.3: Normalized fan- and efficiency curves for axial- and mixed flow fan in open configuration together with system curve

The operating point can be read at the intersection between a fan curve and the system curve. Thus, the axial fan operating point is found at a normalized flow rate of around 0.49, whereas the mixed flow fan operating point is found at a normalized flow rate of 0.52. Then, the fan efficiency at the operating point can be read for each fan by making a straight vertical line from the operating point to the efficiency curve. It can still be said that this efficiency is higher for the axial fan than for the mixed flow fan. Moreover, the axial- and mixed flow fan operating points are equally close to their respective peak efficiency point. Therefore, in this case, the axial fan would perform better than the mixed flow fan.

However, the system curve taken into consideration here is a curve corresponding to a system composed of only two radiators, which would not be the case for a full vehicle. That will be discussed in Section 5.

4.4 Comparison of axial and novel fan concept in ducted configuration

The next step to investigate is a fan performance comparison in the ducted configuration. For this, the two fans and the corresponding computational domain for the ducted configuration is used. The ducted configuration for both the mixed flow fan and the existing axial fan has been compared by generated fan curves for both fans. Figure 4.4 shows the two generated fan curves.

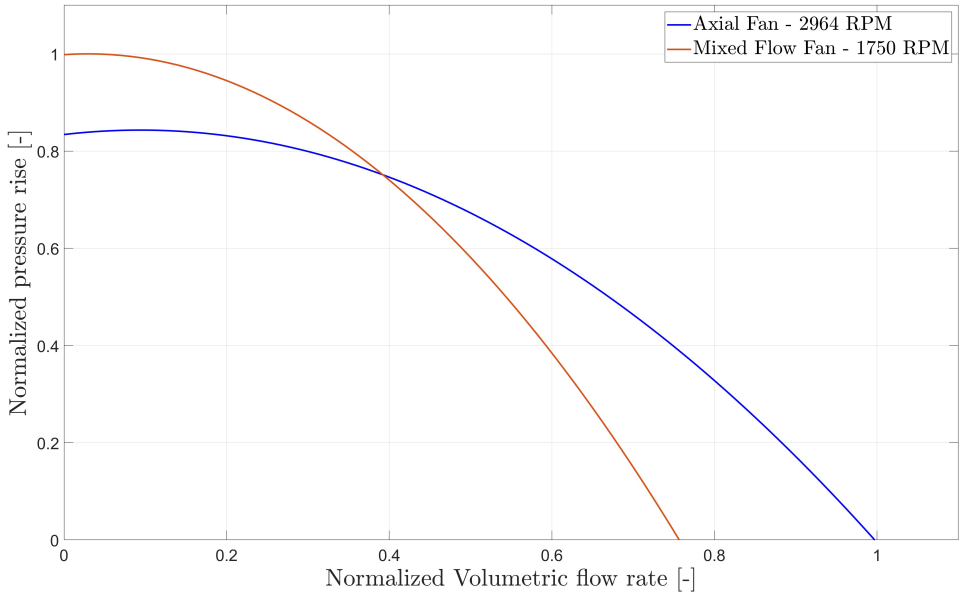

Figure 4.4: Normalized fan curves for axial- and mixed flow fan

It is clear to say that the existing axial fan generates higher mass flows at lower pressure rise, whereas the mixed flow fan overcomes a higher pressure rise for lower flows. The fans definitely have different regimes where performance is higher to one or other.

The efficiency curves are once again plotted for the two fan concepts, and can be seen on Figure 4.5 below:

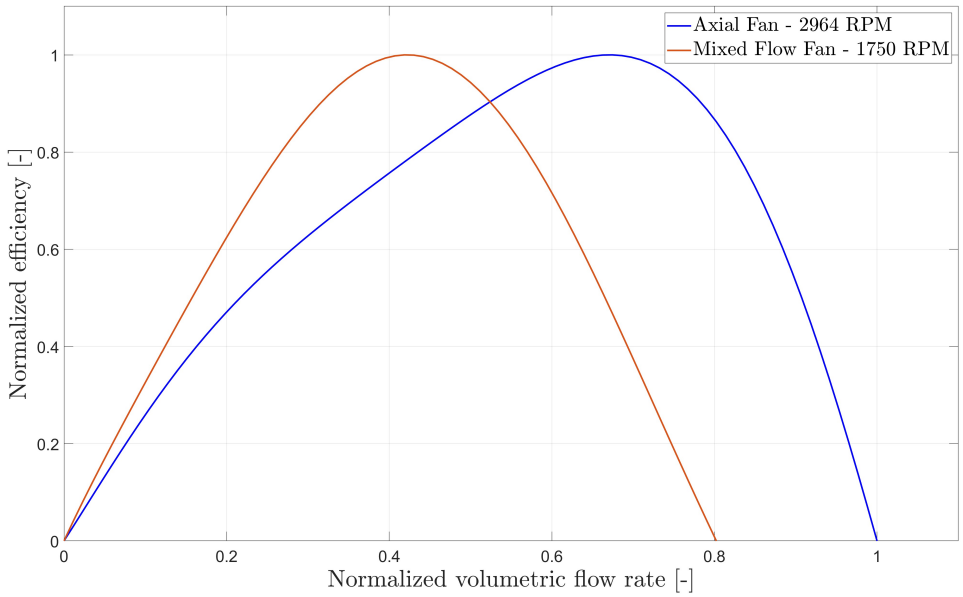

Figure 4.5: Normalized efficiency curves for axial- and mixed flow fan

It is once again clear that the two fan concepts has different flow regime where they perform better. The peak efficiency for axial fan is to the right and for the higher flow regime while the novel fan concepts efficiency curve is more towards the low flow regime.
However, none of these curves, neither fan performance curve nor the efficiency curves can tell which fan will perform better for a certain application without use of a system curve. Existing system curves for two low temperature radiators has been used for finding the operating points.
Figure 4.6 shows the fan and efficiency curves for ducted configuration, together with the system curve.

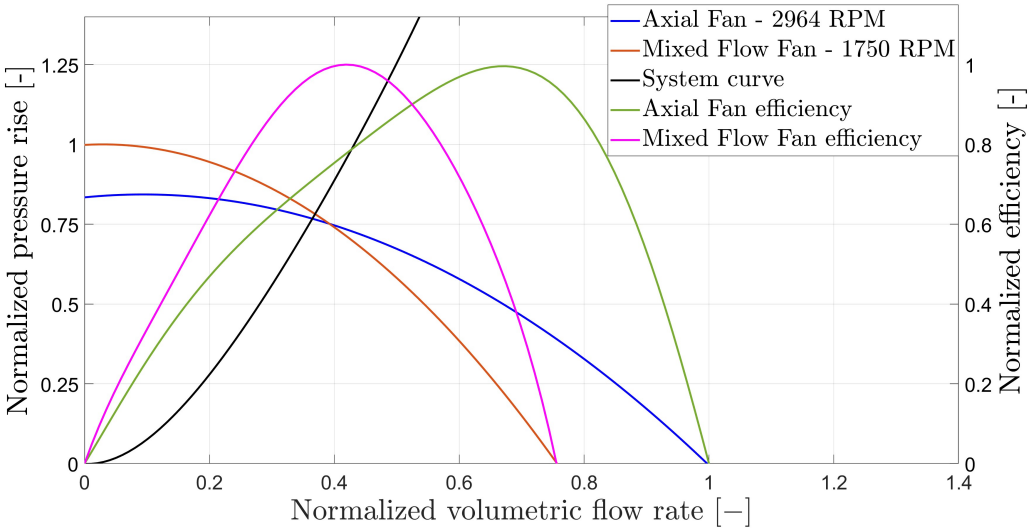

Figure 4.6: All curves

It is shown that the delivered mass flow and corresponding mass flow at this point is very similar for the two fans. With this said the purpose to fulfill, i.e. cooling of coolant is equally well performed. However, the efficiency at this point is higher. This would mean that the two fans deliver the same mass flow, fulfilling the same cooling demand but the novel fan concept uses less energy to do so.

4.5 Ram air simulations with two radiators

However, the fan curves, efficiency curves and system curves presented in previous sections show the fan performance assuming no ram air contribution, i.e., the fan generates the volumetric flow rate. This is, for a car, not the case when driving at speed higher than around 70 kph. When the vehicle moves at these speeds, air is going to pass through shutter openings and move towards the fan. This can, in any figures of the stationary fan curves, be interpreted as pushing more mass, thus a higher volumetric flow rate than the flow at the operating point. The operating point will move towards the right following the respective fan performance curve. Higher volumetric air flow leads to an increase in pressure at the upstream side of the fan, when the increase of pressure is higher than the pressure drop in the system,

the pressure rise is going to be negative, i.e. the fan does not do any useful work.

Figure 4.7 shows the velocity profile for the novel fan concept with a volumetric flow corresponding to a stationary vehicle, i.e., the flow that is generated purely by the fan itself.

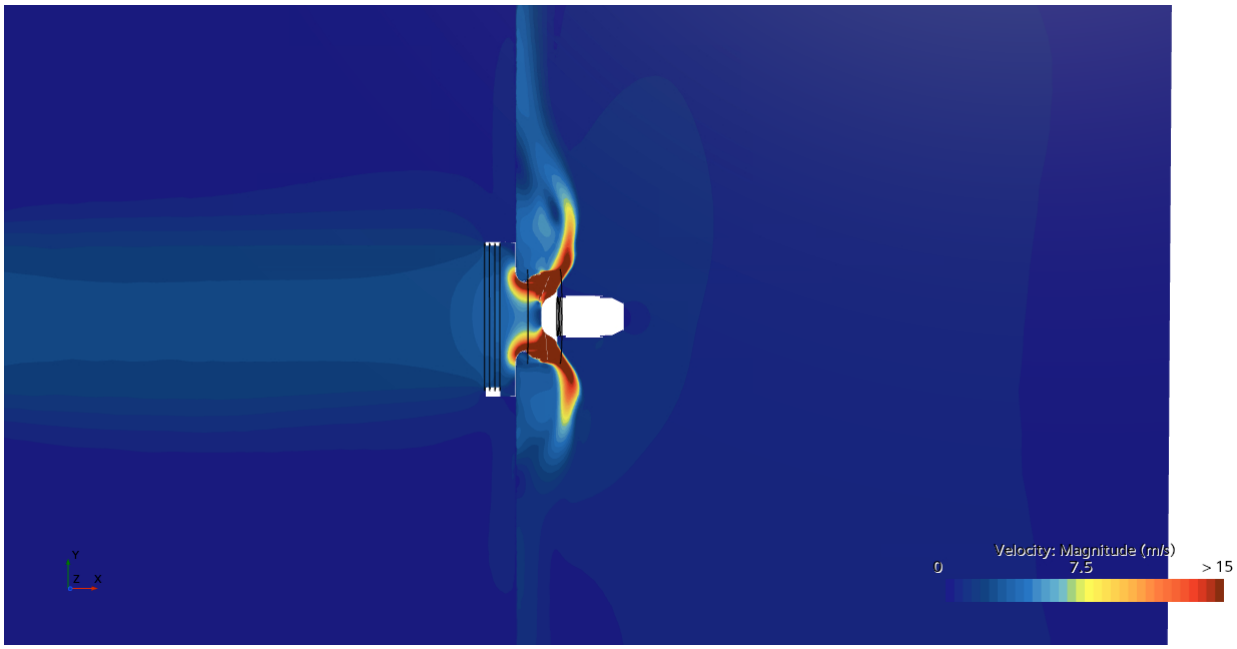

Figure 4.7: Velocity profile of mixed flow fan for 0 kph vehicle speed

The discharge can be seen to be in the radial nature, thus the mixed flow fan concept is preferred at this mass flow. But at higher vehicle speeds and when more mass is pushed towards the fan, the discharge is found to be more axial. Figure 4.8 shows the velocity profile for the novel fan concept for a vehicle speed of around 30kph and the discharge is seen to be more diagonal than the 0kph case.

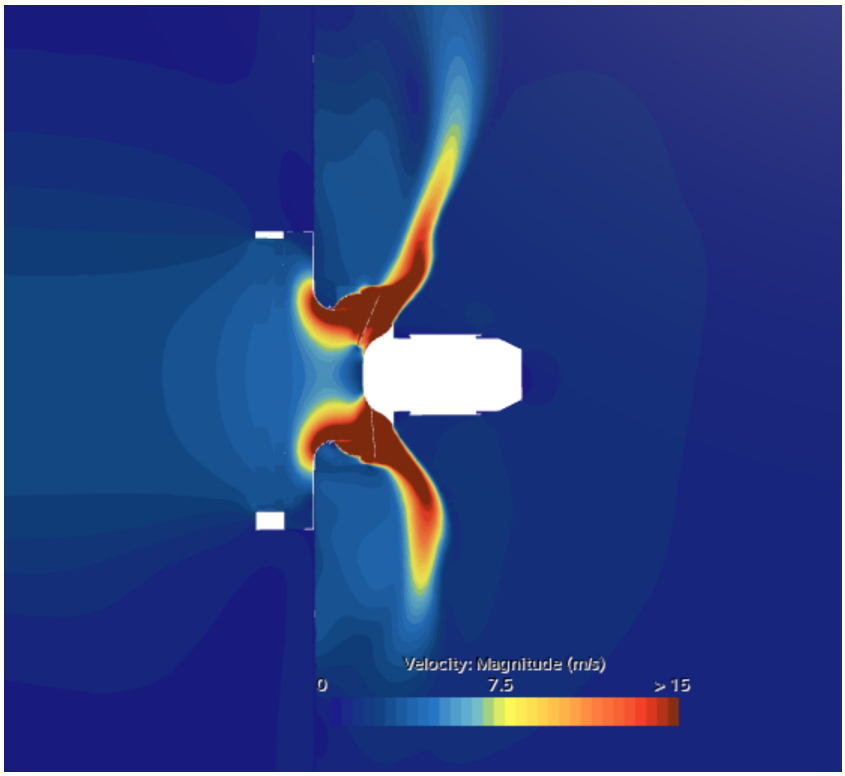

Figure 4.8: Velocity profile of mixed flow fan for 30 kph vehicle speed

Figure 4.9 shows the velocity profile for vehicle speed of 70kph. At this speed the discharge can clearly be seen to be more axial. For this case the efficiency is dropped, and the purpose of diagonal discharge is somewhat lost.

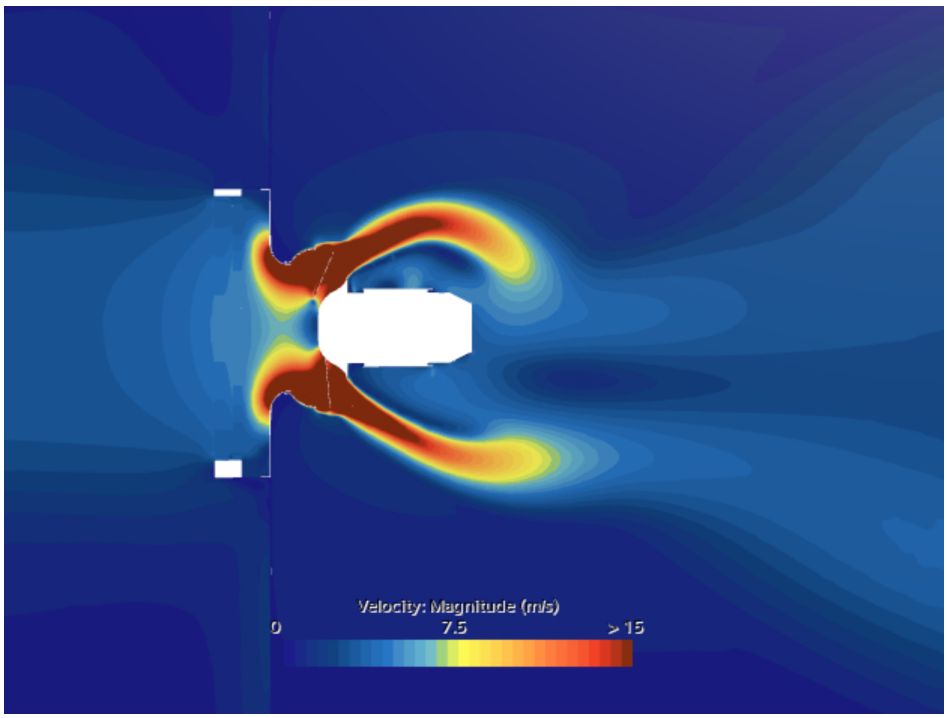

Figure 4.9: Velocity profile of mixed flow fan for 70 kph vehicle speed

Table 4.3 shows a summary of the radial vs axial discharge components in terms of percentage of mass flow leaving the rotating domain.

Table 4.3: Radial and axial discharge rates

Vehicle speed [kph]	Radial mass flow [%]	Axial mass flow [%]
0	43.8	56.2
10	41.4	58.6
30	32.9	67.1
70	3.4	96.6
100	0	100

The efficiency is lowered for higher ram-air i.e., higher vehicle speeds. However, the main target for cooling fans is to provide a sufficient airflow through the radiators to ensure cooling exchange to the coolant. Most often the ram-air contribution is enough to meet the cooling demand but even if the target level of airflow is met, the fan should work at higher vehicle speeds. The novel fan concept offers a higher resistance compared to the existing axial fan and acts as a blockage for the airflow at higher volume flows. For higher vehicle speeds, high mass flow is unavoidable. As there is high resistance from the fan blades and fan shroud, there should be a way to let air through. The proposed solution is speed flaps. Flaps that open at higher mass flows and let air pass the cooling pack. The flaps are not mechanical but made of rubber that open due to the force induced by higher airflows.

Whenever the static pressure measured at the wall of the flaps is negative, they will remain closed, when the static pressure is positive it will result in a force acting normal to the flaps and thus start to open them. Figure 4.10 shows the proposed cooling pack and corresponding static pressure measured at the walls of the pack for different vehicle speeds, and Table 4.4 shows the force acting on the flaps at the different vehicle speeds.

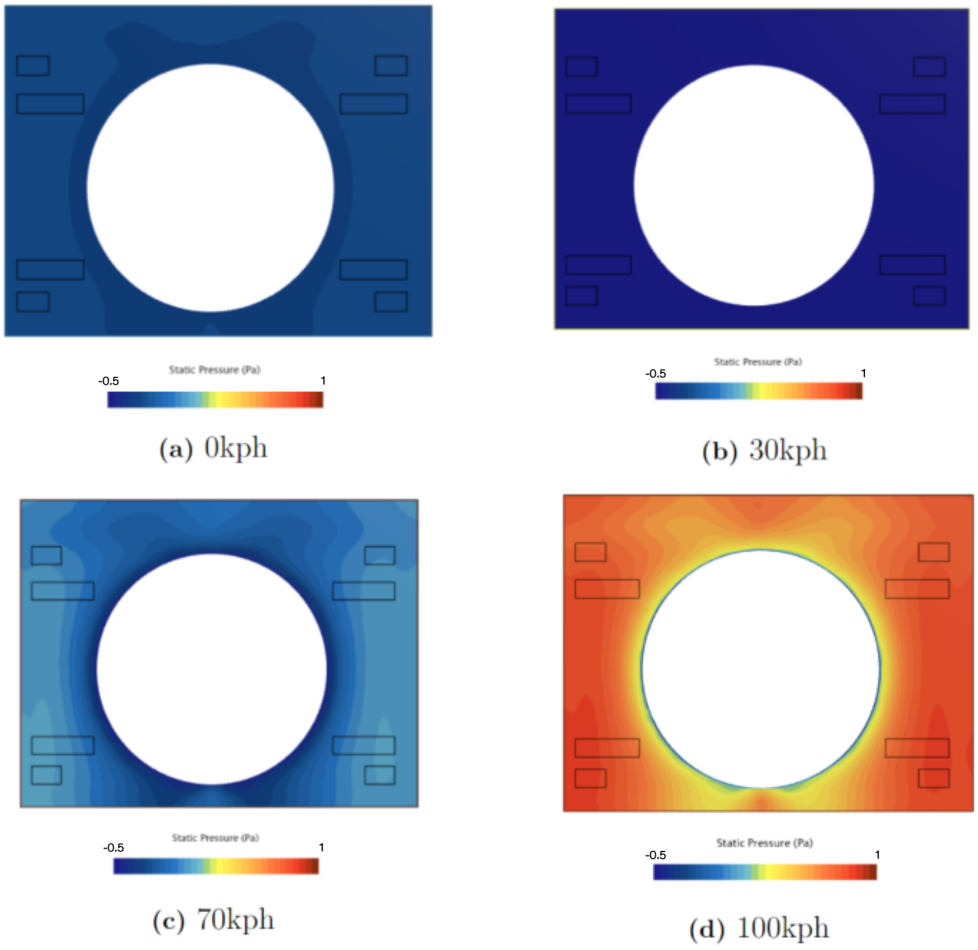

Figure 4.10: Normalized static pressure distribution on cooling pack

Table 4.4: Normalized forces on the flaps for the different vehicle speeds

Vehicle speed	Normalized average force on large flaps	Normalized average force on small flaps
0kph	-0.46	-0.97
30kph	-0.36	-0.76
70kph	0.02	0.02
100kph	0.49	1.00

Up until 30 kph vehicle speed it is clear to say that the flaps will remain closed. Around 70 kph vehicle speed there is a shift in static pressure sign and in force sign, the measured pressure and force at the location of the flaps are shifted to become positive. This will be the start of opening of the flaps. At 100kph there is a large increase both in static pressure and force at the cooling pack wall representing a high ratio of the mass are pushed against the wall instead of flowing through the fan. This will impact the heat exchanger performance at these speeds as it influence the mass flow available for heat exchange at the radiators.

5
Discussion

From the results found in this thesis work, the main idea is that the mixed flow fan is performing better in the ducted configuration as its operating point is located near its peak efficiency point. In this configuration, the axial fan is not as efficient since it operates quite far away from its peak efficiency point.

These findings are only true for the system curve used here, that is, for a system composed of two low temperature radiators. In a real vehicle setup, the system would be composed of more components which would increase the pressure resistance and thus modify the operating point for both fans.

Implementing the full vehicle system curve to the previous results from Sections 4.3 and 4.4, gives the following graphs:

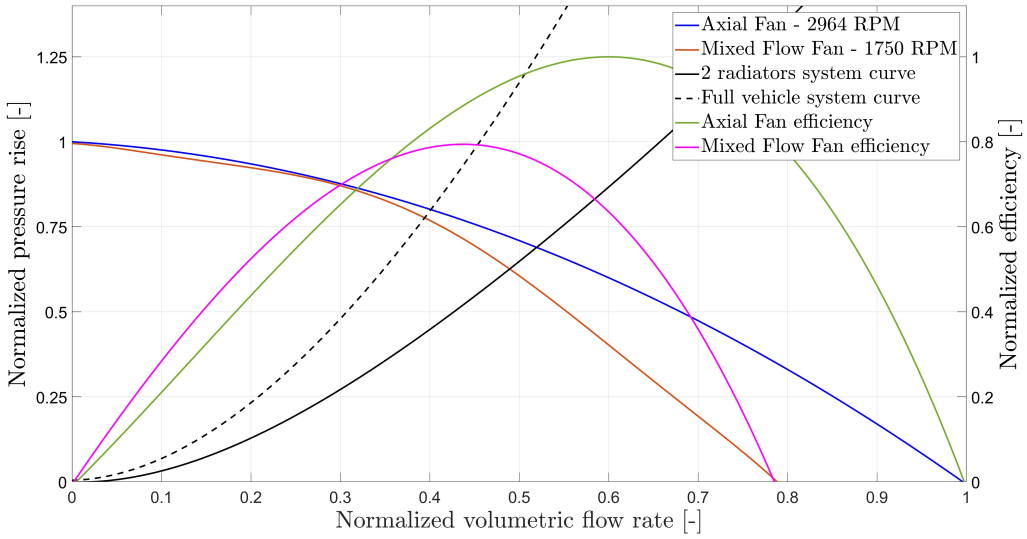

Figure 5.1: Normalized fan- and efficiency curves in open configuration with the full vehicle system curve

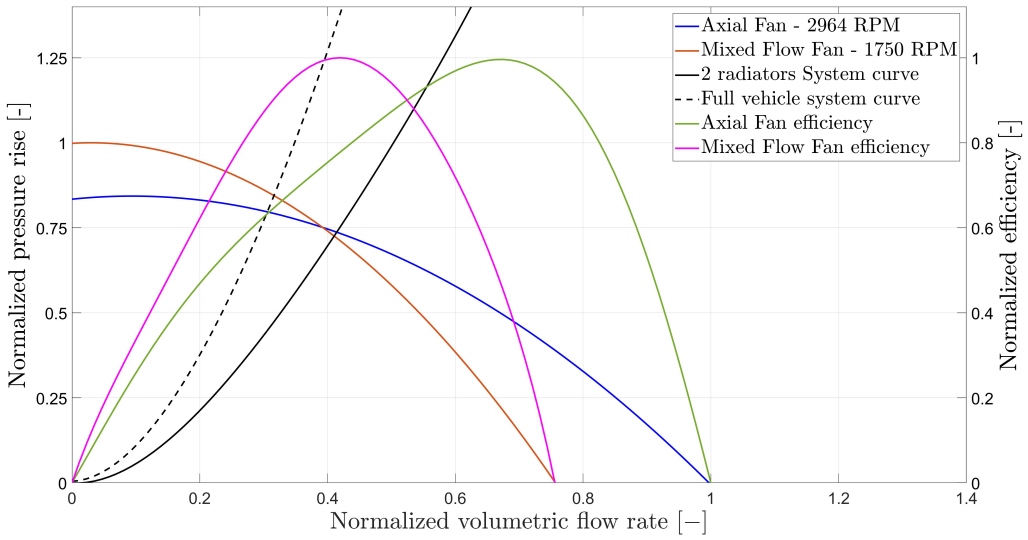

Figure 5.2: Normalized fan- and efficiency curves in ducted configuration with the full vehicle system curve

With these new graphs, it can be seen that, in open configuration, the new operating point is shifted towards lower flows and is now near the peak efficiency point for the mixed flow fan whereas it has moved away from the peak efficiency point of the axial fan, so it is an improvement for the mixed flow fan and a slight decline in axial fan performance. However, the axial fan still operates at slightly higher pressure rise and slightly higher efficiency, which means that it is still a better option than the mixed flow fan in this configuration.

In the ducted configuration, the new operating point is again shifted to lower flows and this time, it has moved away from the peak efficiency point for both fans. It is then a slight decline for the two fans, but the mixed flow fan stays the best option in that case with a higher generated pressure rise and a higher efficiency.

Therefore, even when taking into account the full vehicle system curve, the ducted configuration stays the best configuration to run the mixed flow fan which is good since the configuration inside an electric vehicle is acting more towards a ducted configuration than an open configuration given the tight available place for all the system components.

However, the results given in figure 5.1 and 5.2 is gathered for the open- and ducted configurations respectively. The two types of configurations does not truly correspond to the inside geometry of a vehicle. Open configuration is broadly used across the automotive industry. This thesis is putting effort on shifting focus to the ducted configuration. In order to fully confirm that the mixed flow fan would be preferred when considering full vehicle level simulations, one must first run full vehicle simulations. Doing so would impact the results for fan performance- and efficiency curves. In order to run full vehicle level simulations a new design must be made to fit the fan in its location in the car as the mixed flow fan has different dimensions than the

existing axial fan. For future work with this mixed flow fan concepts, suggestions are made that redesigning of the fan blades would further increase efficiency. Designing the packaging of components and hoses/pipes so that the fan fits the underhood of the car to make it possible to perform full vehicle simulations is also suggested to be done for future work.

6
Conclusion

In this thesis, the mixed flow fan concept has been studied, simulated with CFD and tested in an experimental setup. This novel cooling fan concept has then been compared with the conventional axial fan used in current BEVs at Volvo Cars. It has been found that the two fan concepts have different operating ranges where the two fans are preferred over one other in terms of either efficiency or volume flow delivered. The trend shows, as the literature review expected, that the mixed flow fan is preferred in the lower mass flow region and the axial fan is preferred in the region of higher mass flows. However, the type of configuration also influences the results. This thesis has focused on two types of configurations, open- and ducted configuration, corresponding to the experimental setups used in fan test rigs according to the ISO 5801 standard.
It has been seen that, even if the axial fan is better performing than the mixed flow fan in open configuration while the vehicle is standing still, the mixed flow fan is more efficient and thus preferable in ducted configuration for the still condition. The mixed flow fan can even almost catch up the axial fan in terms of performance in open configuration when the pressure resistance of the full vehicle is taken into account.
However, the vehicle is not always static, and some simulations have been performed to study the impact of vehicle speed. It has therefore been seen that the faster the car goes, the less efficient the fan becomes as it starts to work in the axial regime, and the more airflow is being blocked by the fan acting as a resistance which prevent the radiators to be cooled down properly. A solution has been found for that and speed flaps can be installed on the shroud to let the flow circulate.
All these points show that the mixed flow fan is promising for the automotive industry and further studies need to be conducted to evaluate it.

Bibliography

[1] D. Gebert, "A NOVEL AXIAL FAN CONCEPT DEVELOPED USING PARAMETRIC OPTIMIZATION," ebm-papst Mulfingen GmbH & Co., Senlis, France, 2022.

[2] K. Shimada, T. Kuriwada, T. Sakai and K. Ohyama, "Design of Aerodynamic Diagonal Flow Fan for Engine Cooling," SAE International, Warrendale, PA, USA, SAE Technical Paper 980059, 1998.

[3] T. Kawano and M. Fuchiwaki, "Aerodynamic performances and efficiency of axial flow fan placed in cooling system," *J. Phys.: Conf. Ser.* 2217 012002, 2022, doi: 10.1088/1742-6596/2217/1/012002.

[4] S. Zhou, L. Lu, B. Xu, J. He and D. Xia, "Performance Optimization Design of Diagonal Flow Based on Ensemble of Surrogates Model," *Appl. Sci.* 2022, 12, 9732, Sept. 2022, doi: 10.3390/app12199732.

[5] R. Franzke, S. Sebben, T. Bark, E. Willeson and A. Broniewicz, "Evaluation of the Multiple Reference Frame Approach for the Modelling of an Axial Cooling Fan," *Energies* 2019, 12, 2934, Jul. 2019, doi: 10.3390/en12152934.

[6] B. Andersson et al., *Computational Fluid Dynamics for Engineers*, Cambridge, UK: Cambridge University Press, 2012.

[7] Siemens Digital Industries Software, Simcenter STAR-CCM+ User Guide, Version 2022.1, In *Reference Frames*, Siemens, 2022.

[8] O. Fares, "Numerical Investigation of Noise Generation by Automotive Cooling Fans," MSc thesis, Department of Mechanics and Maritime Science, Chalmers University of Technology, Gothenburg, Sweden, 2019.

[9] *Fans - Performance testing using standardized airways*, SS-EN ISO 5801:2017, Swedish Institute for Standards, Stockholm, Sweden, 2017.

[10] *Understanding Fan Curves - Fe-2000.*, Minneapolis, MN, USA: Twin City Fan Companies Ltd., 2018.

[11] P.V. Gullberg, "Optimisation of the Flow Process in Engine Bays - 3D Modelling of Cooling Airflow," Ph.D. thesis, Department of Applied Mechanics, Chalmers University of Technology, Gothenburg, Sweden, 2011.

DEPARTMENT OF SOME SUBJECT OR TECHNOLOGY
CHALMERS UNIVERSITY OF TECHNOLOGY
Gothenburg, Sweden
www.chalmers.se

CHALMERS
UNIVERSITY OF TECHNOLOGY